Tropical Instability Waves as a Resonance between Equatorial Rossby Waves*

JOHN M. LYMAN

NOAA Pacific Marine Environmental Laboratory, Seattle, Washington

DUDLEY B. CHELTON, ROLAND A. DESZOEKE, AND ROGER M. SAMELSON

College of Oceanic and Atmospheric Sciences, Oregon State University, Corvallis, Oregon

(Manuscript received 24 December 2003, in final form 24 June 2004)

ABSTRACT

To understand the characteristics of sea surface height signatures of tropical instability waves (TIWs), a linearized model of the central Pacific Ocean was developed in which the vertical structures of the state variables are projected onto a set of orthogonal baroclinic eigenvectors. In lieu of in situ current measurements with adequate spatial and temporal resolution, the mean current structure used in the model was obtained from the Parallel Ocean Climate Model (POCM). The TIWs in the linear model have cross-equatorial structure and wavenumber–frequency content similar to the TIWs in POCM, even when the vertical structures of the state variables are projected onto only the first two orthogonal baroclinic eigenvectors. Because this model is able to reproduce TIWs with relatively simple vertical structure, it is possible to examine the mechanism for the formation of TIWs. TIWs are shown to form from a resonance between two equatorial Rossby waves as the strength of the background currents is slowly increased.

1. Introduction

Tropical instability waves (TIWs) are a dominant feature of monthly variability in the equatorial Pacific and Atlantic Oceans. Here we set out to examine their cross-equatorial structure and origins in the central Pacific as observed in sea surface height (SSH).

The large-scale structure of TIWs in the Pacific was first characterized by Legeckis (1977) from a geostationary satellite measuring sea surface temperature (SST). Cusps in the northern equatorial front within a few degrees north of the equator were observed with periods of about 25 days and wavelengths of about 1000 km. Since then, TIWs have been observed remotely in satellite measurements of sea surface heights (Malardé et al. 1987; Musman 1989; Périgaud 1990; Weidman et al. 1999; D. B. Chelton et al. 2004, unpublished manuscript, hereinafter CSLD), wind (Xie et al. 1998; Chelton et al. 2001; Hashizume et al. 2001), ocean color (Strutton et al. 2001), as well as SST (Legeckis et al. 1983; Legeckis 1986; Pullen et al. 1987; Chelton et al. 2000; Contreras 2002). TIWs have also been observed in in situ measurements of velocity (Harvey and Patzert 1976; Wyrtki et al. 1981; Hansen and Paul 1984; Halpern et al. 1988; McPhaden 1996; Baturin and Niiler 1997; Kennan and Flament 2000) and temperature measurements (Menkes et al. 1996; McPhaden 1996; Flament et al. 1996; Kennan and Flament 2000). These observations variously estimate the period and wavelength of TIWs to be in the ranges of 15–40 days and 800–2000 km, respectively. The broad ranges for the periods and wavelengths of TIWs are partly due to the complicated forcing of the instabilities, which has been shown in modeling (Philander 1978; Cox 1980; Proehl 1998; McCreary and Yu 1992; Donohue and Wimbush 1998; Masina et al. 1999a) and observational studies (Hansen and Paul 1984; Luther and Johnson 1990; Qiao and Weisberg 1998) to have both baroclinic and barotropic contributions that vary in time, longitude, and latitude.

Linear models of mean ocean conditions give insight into the origins of TIWs that cannot be easily deduced from the complicated energetics of fully nonlinear solutions. The general characteristics of TIW signatures in SST north of the equator were reproduced by Philander (1978) in a two-layer, reduced-gravity model that was linearized about an idealized representation of the equatorial current system consisting of a broad South Equatorial Current (SEC) and a North Equato-

* Pacific Marine Environmental Laboratory Contribution Number 2562.

Corresponding author address: John M. Lyman, Pacific Marine Environmental Laboratory, NOAA/R/PMEL, 7600 Sand Point Way, Seattle, WA 98115.
E-mail: john.lyman@noaa.gov

rial Countercurrent (NECC) centered on 5°N. It is noteworthy that the mean current considered by Philander (1978) did not include the effects of the Equatorial Undercurrent (EUC), which splits the SEC into two branches of westward flow. The eigenvectors corresponding to the fastest-growing modes had a wavelength of 1000 km and a period of 30 days, which are similar to the observed values reported by Legeckis (1977) and Legeckis et al. (1983), and were restricted in amplitude to the region north of the equator. These solutions were barotropically unstable, drawing energy from the meridional shear between the SEC and NECC.

Investigating the origins of TIWs in a three-layer, reduced-gravity nonlinear model, McCreary and Yu (1992) considered a version of their model that was linearized about the mean current structure from the fully nonlinear model. The nonlinear version of the model produced three unstable modes, two of which were antisymmetric in pressure while the other was symmetric in pressure with a period of 28 days and a wavelength of 1100 km. The linearized model was able to reproduce the two antisymmetric modes in pressure but was unable to represent the symmetric mode accurately, producing symmetric solutions with periods of 22 days and 766-km wavelengths.

A more detailed look at the energetics in the three-layer, reduced-gravity linearized model was presented by Yu et al. (1995) in an attempt to understand why TIWs have largest amplitudes north of the equator. By altering an idealized mean current structure, they showed that the two antisymmetric modes are affected by cross-equatorial asymmetries in the SEC and the equatorial SST fronts, while the existence of the NECC had little or no effect on the symmetry of the solutions. Reductions in the southern branch of the SEC (SECS), and the south equatorial front led to unstable solutions with larger amplitude north of the equator. These solutions had slower growth rates and dispersion characteristics that are similar to those from a symmetric background mean state. The energy sources for the TIWs were found to consist of both frontal and barotropic instabilities.

Expanding the vertical resolution of a previous linear stability analysis, Proehl (1998) looked at the effect of asymmetries in the background flow on the stability of a 20-layer equatorial β-plane model. Although the shears on both sides of the north branch of the SEC (SECN) were found to be potentially unstable, the barotropic instabilities on the southern side of the SECN were the primary energy source for the TIWs. A physical description was presented in terms of what Proehl (1998) referred to as wave overreflection, which was able to explain the origins of the TIWs in terms the location of critical layers and surfaces of zero potential vorticity gradients. The most unstable solutions had maximum amplitudes within a few degrees of the equator, periods between 30 and 35 days, and wavelengths around 800–900 km.

Besides wavenumber–frequency content, TIWs can also be identified by their cross-equatorial structure. The latitudinal structure is most readily observed in satellite measurements of SST and SSH, which resolve TIWs in synoptic images with large spatial scales. SSH provides a more dynamical estimate of the cross-equatorial structure. From the Ocean Topography Experiment (TOPEX)/Poseidon, the cross-equatorial structure of the SSH signatures of TIWs have been observed to have maxima at about 5°N and 5°S with about a factor-of-2 larger amplitude north of equator (CSLD). The southern maxima are found have a tendency to be in phase with the northern maxima, but the relative phase varies somewhat over the course of a TIW season. The relative amplitude and phase of the secondary maximum in the SSH signatures of TIWs south of the equator have not been explained by the previous linear stability analyses.

In this study, we take a different approach from earlier linear stability analyses. Rather than representing the vertical structure of the state variables u, v, and p by discrete layers, the state variables are projected onto a set of vertical baroclinic eigenvectors. This method produces a simple model of TIWs in which, unlike a layered model, the mean is not based on an arbitrary vertical averaging scheme. It also allows for the identification of points in wavenumber–frequency space where equatorially trapped Rossby waves resonate to form an unstable solution. TIWs are identified in this model by their wavenumber–frequency content and their cross-equatorial structure in SSH, contrasting previous analyses that have generally focused on u and v.

Because in situ observations of the mean zonal currents with adequate spatial and temporal resolution do not exist, we consider the stability of a mean current profile in the central equatorial Pacific from the Parallel Ocean Climate Model (POCM). POCM has been previously shown to reproduce realistic TIWs (Semtner and Chervin 1992; Stammer 1997; McClean et al. 1997; Kennan and Flament 2000; Weidman et al. 1999). For consistency, the TIW characteristics deduced from the linear stability analysis are compared with the TIWs in POCM model output rather than with the TOPEX/Poseidon observations.

The structures of TIWs in POCM are identified in section 2. The details of the projection model are derived in section 3. TIWs are investigated from single-, two-, and five-mode projection models in section 4 based on a mean current profile from POCM. It is shown in section 4 that two modes are sufficient to describe the dynamics of TIWs. The two-mode projection model is used in section 5 to examine the origins of the TIWs in terms of a resonance of two equatorial Rossby waves.

2. POCM

As noted in the introduction, the existence of monthly variability associated with TIWs in POCM has previously been discussed in several studies. Of particular interest, Kennan and Flament (2000) compared the vertical structure of a TIW from POCM with in situ observations of an individual vortex in the westward-propagating TIW wave train and found good agreement between the distributions of the modeled and observed divergence and relative vorticity fields. This suggests that the dynamics of TIWs can be investigated from the POCM simulation.

Monthly variability of SSH in POCM consists of westward-propagating, latitudinally asymmetric waves with larger amplitudes north of the equator. This asymmetry can be seen in the map standard deviation of SSH measurements from POCM that have been filtered to retain periods between 25 and 60 days (Fig. 1). Two bands of high SSH variability straddle the equator at about 5°N and 5°S. In POCM, the variability extends beyond the date line to 170°E in the south and extends all the way to the western boundary in the north. In the east, the POCM variability does not appear until 120°W in the north and 130°W in the south (Fig. 1).

Time–longitude plots of 5 yr of filtered SSH along 5°N (Fig. 2) show annual and interannual variability in the amplitudes of the TIW signals, with SSH signals that are weak to nonexistent during the 1997/98 El Niño and strong during the 1995/96 La Niña. During the 1995/96 TIW season, time–longitude plots of POCM SSH along 5°N are similar in amplitude, longitudinal extent, and duration to TOPEX/Poseidon observation of SSH (Fig. 2). For this reason, and because the 1995/96 TIW season was strong in POCM, this time period was chosen for the linear-stability analysis of POCM. In particular, the mean fields were computed along 134°W during the beginning of the TIW season, from 8 July 1995 to 6 September 1995, before the TIWs became fully developed, so that the assumption of linearity is still valid.

Spectral estimates from time–longitude plots of POCM variability at 5°N yield a period and wavelength of the TIWs of about 28 ± 2 days and 1350 ± 150 km, respectively. The uncertainties in these period and wavelength estimates are derived from the Fourier frequency and wavenumber intervals based on the zonal span from 160°E to 100°W and the record length from June 1995 to June 1996 over which the spectrum was computed.

The version of the POCM analyzed here is run 4C. It is a 1/4°-resolution, 20-level model with 30-min time step forced by 3-day European Centre for Medium-Range Weather Forecasts (ECMWF) renanalysis wind stress and heat flux fields (R. Tokmakian 1999, personal communication). The POCM SSH and velocity fields used in this analysis were averaged over 3 days. For more details on POCM, see Semtner and Chervin (1992). The mean zonal currents and the latitudinal structure of TIWs near 134°W in POCM are described in sections 2a and 2b, respectively.

a. The mean zonal current near 134°W

The mean zonal current used in the linear stability analyses in section 3 is defined to be the average over 60 days centered on 8 August 1995 and 14° in longitude centered at 134°W. This corresponds to about two periods and one wavelength of the TIW variability in POCM. This region was chosen because it corresponds to the geographical location where TIWs form in POCM (see Fig. 1). This time period was chosen be-

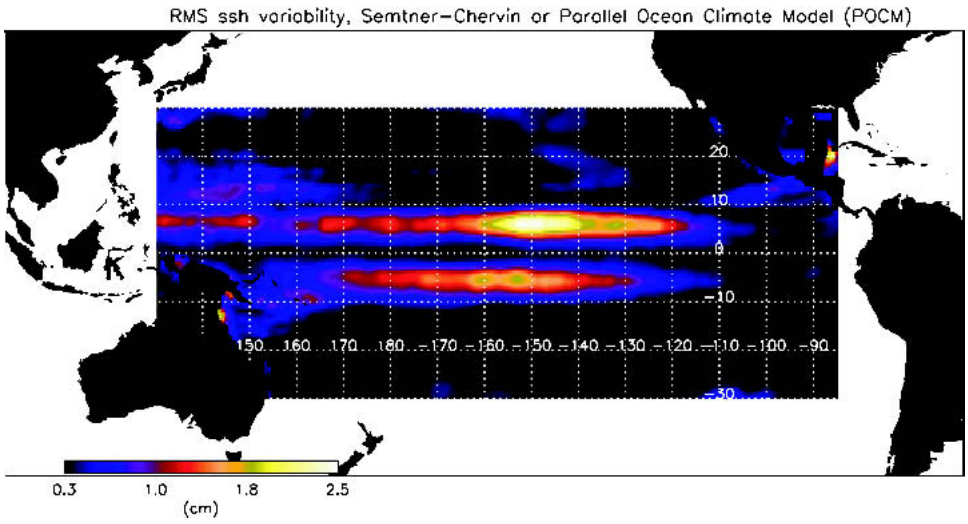

FIG. 1. The standard deviation of SSH from POCM filtered to retain periods between 25 and 60 days, computed over the 5-yr period of Nov 1992–Oct 1997.

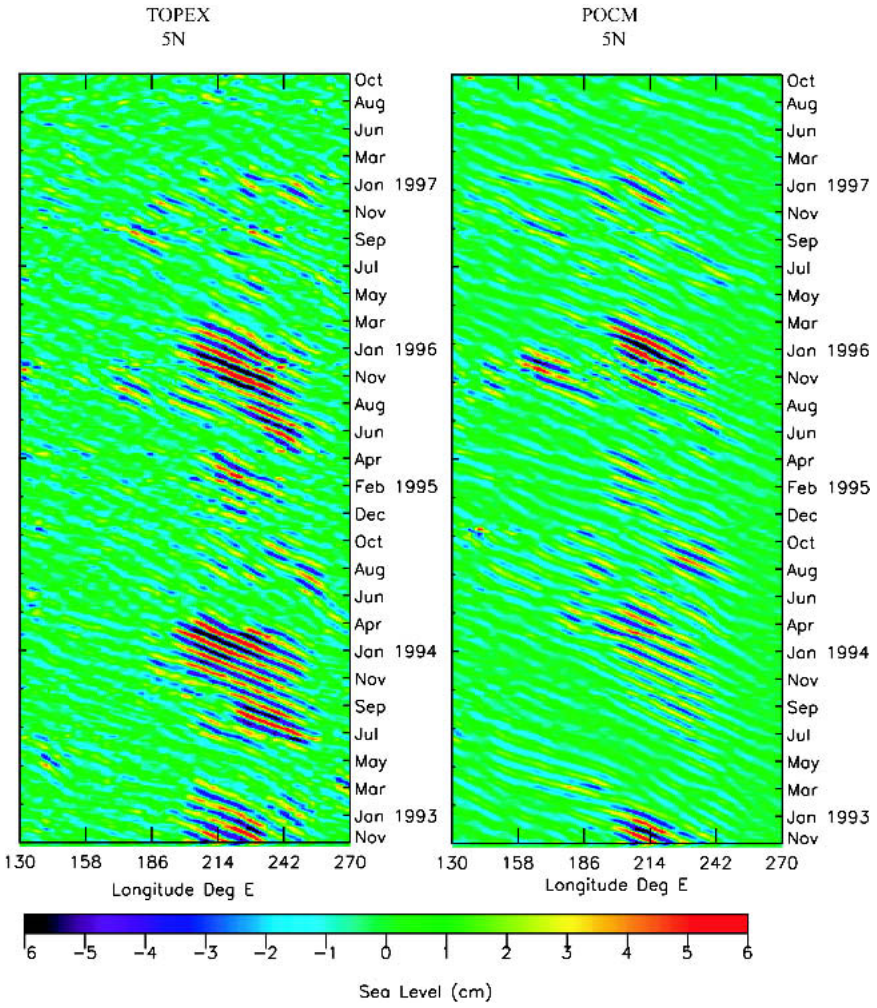

FIG. 2. Time–longitude plots along 5°N of SSH filtered to retain periods between 25 and 60 days for (left) TOPEX and (right) POCM.

cause it coincides with a La Niña event during which TIWs are generally most energetic (Baturin and Niiler 1997). As noted above, the 1995 La Niña in particular was chosen because the monthly SSH signal in the POCM record was similar to TOPEX observations (see Fig. 2).

The POCM mean zonal current structure (Fig. 3) contains all of the components of the equatorial current system that are thought to be important in the formation of TIWs. There is an EUC, NEC, SECN, and SECS, all of which contain strong vertical and meridional shears.

b. The cross-equatorial structure of TIWS near 134°W

The characteristics of TIWs are known to vary both geographically and temporally over the course of a 9-month TIW season (Philander et al. 1986; Luther and Johnson 1990; Masina et al. 1999b; CSLD). These variations can be quantified by a wavelet decomposition, which is similar to a Fourier decomposition, except that the decomposition is over a set of specified basis functions (wavelets) that are localized in both time and frequency space, rather than the set of sine and cosine functions (Mallat 1999). The structure of the wavelet used in the decomposition is chosen to resemble the structure of the signal of interest. The Morlet wavelet, which is a Gaussian tapered sine and cosine (middle panel, Fig. 4), resembles the temporal variability of TIWs (top panel, Fig. 4) and is described mathematically by

$$W_s(t) = \frac{1}{\pi S^2} e^{i(mt/S)} e^{-(1/2)(t/S)^2}, \quad (1)$$

where t is time, S characterizes the temporal scale of the wavelet, and m is the order of the wavelet, which characterizes the number of sinusoidal oscillations within an e-folding scale. For the analysis presented here, the or-

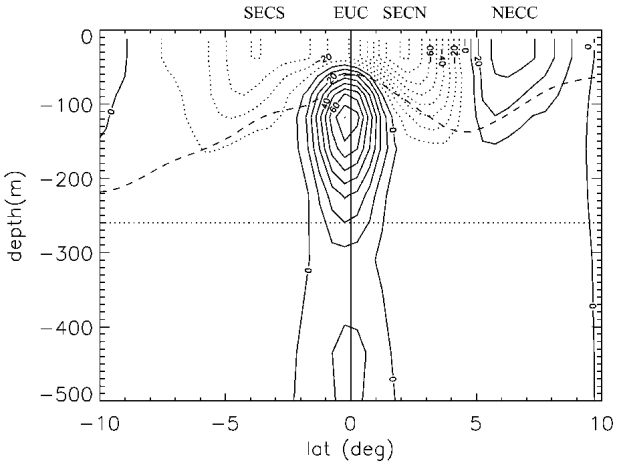

FIG. 3. A contour plot of the mean currents (cm s^{-1}) from POCM at 134°W, averaged during the early period of the 1995/96 TIW season (8 Jul–6 Sep 1995). The two lines represent options for arbitrary vertical averaging of the currents. The dotted line is the 260-m isobath and the dashed line is the depth of the 20° isotherm.

der of the wavelet was held constant at $m = 3$. The frequency of the wavelet is m/S and the e-folding time is $S\sqrt{2}$. By representing SSH by Morlet wavelets and identifying the wavelet scale S with the largest amplitude, it is possible to quantify the temporal variations of TIW periodicity and meridional structure.

The amplitude of fit of a particular wavelet at a time t is given by

$$A_S(t) = \frac{\int h(u)W_s(u - t)\,du}{\int |W_s(u)|^2\,du}. \qquad (2)$$

In the case presented in this section, $h(t)$ represents the time series of SSH. Because $W_s(t)$ is complex, so is the resulting time series, $A_S(t)$, which gives the amplitude and phase of the wavelet fit. These two pieces of information are used later in this section to determine the cross-equatorial structure of the phase and amplitude of the TIWs.

The $m = 3$ Morlet wavelets were fit to the filtered SSH signal along 5°N, 134°W (top panel, Fig. 4) at each successive 3-day time step. The process was repeated for wavelet time scale S corresponding to periods ranging from 20 to 40 days in 1-day increments. At each 3-day time step, the period S/m that described the greatest amount of variance was chosen to represent SSH (bottom panel, Fig. 4). The small span of the exponentially decaying envelope as compared with the periodicity of the Morlet wavelet allows for higher resolution of the temporal variations of the structure of the signal. The down side of the small envelope is poor frequency resolution (Mallat 1999). The plot of the period as a function of time is therefore only a rough guide to the frequency content of the signal, and we do not consider the small variation in periodicity in the bottom panel of Fig. 4 to be significant.

The scale of the Morlet wavelet with the largest amplitude at 5°N, 134°W was used to characterize the meridional structure of SSH as a function of time. For a given time, this best-fit wavelet at 5°N was fit to the SSH time series at each latitude along 134°W (Fig. 5). This decomposition describes more than 70% of the variance along given latitude in the 25–60-day bandpass-filtered SSH between the equator and 8°N, and about 40% of the variability between about 2° and 8°S (bottom-right panel, Fig. 5). The smaller amount of the variance described in the south by the wavelet decomposition is largely due to the small amplitude of the signal in the south during July–August 1995. Over the extended 12-month time period July 1995–July 1996, the percent of the variance described in the south increases to about 70% (see top-right panel in Fig. 5). Hence, the wavelet analysis is a good descriptor TIWs.

The wavelet decomposition quantities the time variability that is visually apparent in the time–latitude plots of SSH (Fig. 5). The amplitude of these variations is about a factor of 5 larger along 5°N than along 5°S in early July. The asymmetry decreases to about a factor of 3 by the end of August. The "tilting" near the equa-

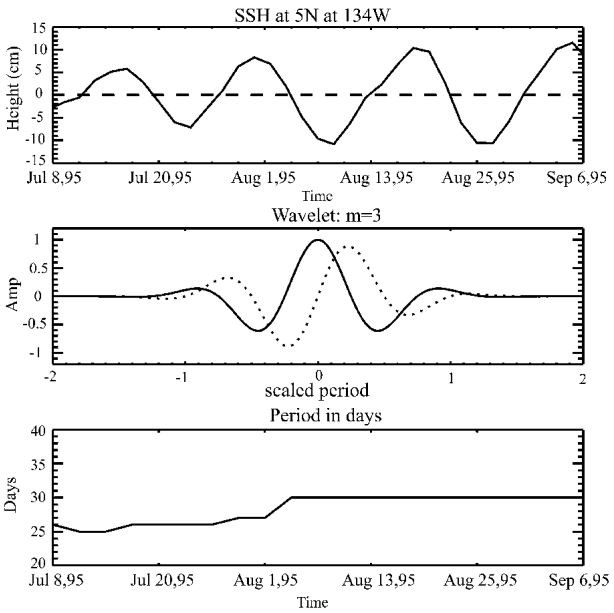

FIG. 4. The wavelet decomposition of filtered SSH from POCM. (top) A slice of filtered SSH at 5°N, 134°W during the early period of the 1995/96 TIW season. (middle) A plot of the $m = 3$ Morlet wavelet that was fit to SSH. The solid and the dashed lines are the Gaussian tapered cosine and sine functions of the Morlet wavelet. Wavelets with different periods, i.e., different scales (S), were fit to SSH for each time. (bottom) The period of the wavelet with the best fit to SSH as a function of time.

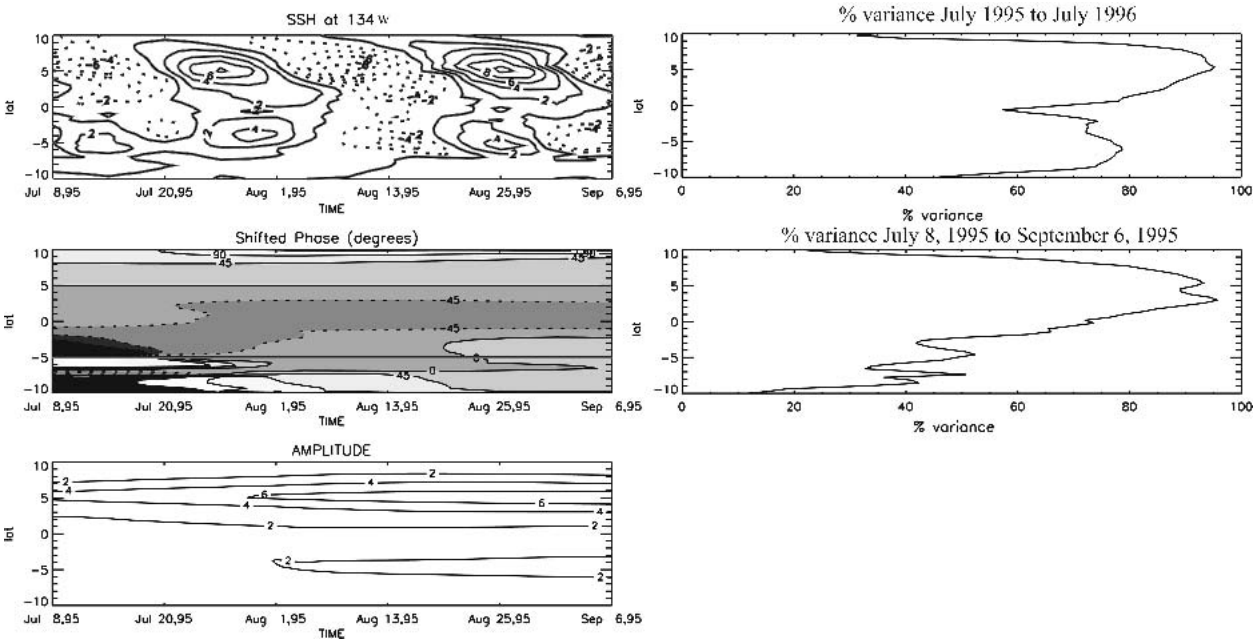

FIG. 5. The decomposition of filtered SSH from POCM into phase and amplitude as a function of time and latitude. (top left) A time–latitude plot of the SSH along 134°W during the early period of the 1995/96 TIW season. At each 3-day time step, the best-fit wavelet at 5°N (Fig. 4) was fit to SSH at each latitude. (middle left) The phase of the wavelet fit relative to the phase at 5°N. (bottom left) The amplitude of the wavelet fit (cm). (top right) A plot of the percentage of SSH variance explained by the $m = 3$ wavelet over the period Jul 1995–Jul 1996. (bottom right) A plot of the percentage of SSH variance explained by the wavelet over this 2-month record.

tor in the SSH signal represents a phase lag of about 45° at the equator relative to 5°N (second panel of Fig. 5). This tilting is evidence of barotropic energy conversion (see section 4). The phase lag of SSH at 5°S relative to 5°N varies from 45° in late July to 0° in August.

3. The projection model

For the model used in this paper, the vertical dependence of the state variables u, v, and p in a continuously stratified model are projected onto a set of vertical baroclinic eigenfunctions (see appendix A). This is possible because the solutions of Sturm–Liouville eigenvalue problem that defines the set of vertical baroclinic eigenfunctions functions are orthogonal and span the space subject to their boundary conditions (Guenther and Lee 1988). The method of projecting the continuous model onto the baroclinic eigenfunctions is described in this section. The full three-dimensional continuous model is described in section 3a. In section 3b, the continuous set of equations is projected onto the vertical eigenfunctions, integrated, and truncated such that the results yield a set of equations representative of the first baroclinic mode, which are not subject to an arbitrary averaging scheme. In section 3c, the formalism of the projection model is expanded to include an arbitrary number of baroclinic modes.

a. The continuous model

The continuous, three-dimensional equations at the equator subject to a rigid lid, a flat bottom, the Boussinesq approximation, and linearization about a mean background zonal current $U_o(y, z)$ and the associated geostrophically balanced mean background density $\rho_o(y, z)$ are

$$\left(\frac{\partial}{\partial t} + U_o\frac{\partial}{\partial x}\right)u + \left(\frac{\partial U_o}{\partial y} - \beta y\right)v + \frac{1}{\rho_*}\frac{\partial}{\partial x}p + \frac{\partial U_o}{\partial z}w = 0, \tag{3}$$

$$\left(\frac{\partial}{\partial t} + U_o\frac{\partial}{\partial x}\right)v + \beta y u + \frac{1}{\rho_*}\frac{\partial}{\partial y}p = 0, \tag{4}$$

$$\left(\frac{\partial}{\partial t} + U_o\frac{\partial}{\partial x}\right)\rho + \frac{\partial \rho_o}{\partial y}v + \frac{\partial \rho_o}{\partial z}w = 0, \tag{5}$$

$$\frac{\partial}{\partial x}u + \frac{\partial}{\partial y}v + \frac{\partial}{\partial z}w = 0, \quad \text{and} \tag{6}$$

$$\rho = \frac{-1}{g}\frac{\partial}{\partial z}p. \tag{7}$$

In the above equations, x is the zonal coordinate, y is the meridional coordinate, z is the vertical coordinate, u is the perturbation zonal velocity, v is the perturba-

tion meridional velocity, w is the perturbation vertical velocity, p is the perturbation pressure, ρ is the perturbation density, ρ_o is the mean background density structure, and ρ_* is the constant reference background density. Equations (3)–(7) are subject to the following boundary conditions:

$$v = 0 \text{ at the northern and southern boundaries} \quad (8)$$

and

$$w = 0 \text{ at the top and bottom boundaries.} \quad (9)$$

In linearizing the equations about a mean background density structure, it is assumed that

$$\text{density} = \rho_* + \rho_o(y, z) + \rho(x, y, z, t). \quad (10)$$

It is also assumed that $\rho_o(y, z)$ is a weakly varying function of y:

$$\rho_o(y, z) = \rho_1(z) + \varepsilon\rho_2(y, z), \quad (11)$$

where $\varepsilon \ll 1$.

Equations (3)–(7) can be combined to obtain a single equation in terms of any one of the state variables. However, there are extraneous roots to this equation (Proehl 1991). To avoid these extraneous roots, (3)–(7) can be rewritten in terms of a coupled set of three equations involving the three state variables u, v, and p, as suggested by Proehl (1998). The resulting equations are

$$\left(\frac{\partial}{\partial t} + U_o\frac{\partial}{\partial x}\right)u + \left(\frac{\partial U_o}{\partial y} - \beta y + \frac{g}{\rho_* N^2}\frac{\partial U_o}{\partial z}\frac{\partial \rho_o}{\partial y}\right)v + \left[\frac{1}{\rho_*}\frac{\partial}{\partial x} + \frac{-1}{\rho_* N^2}\frac{\partial U_o}{\partial z}\left(\frac{\partial}{\partial t} + U_o\frac{\partial}{\partial x}\right)\frac{\partial}{\partial z}\right]p = 0, \quad (12)$$

$$\left(\frac{\partial}{\partial t} + U_o\frac{\partial}{\partial x}\right)v + \beta y u + \frac{1}{\rho_*}\frac{\partial}{\partial y}p = 0, \quad \text{and} \quad (13)$$

$$\frac{\partial}{\partial x}u + \left[\frac{\partial}{\partial y} + \frac{\partial}{\partial z}\left(\frac{g}{\rho_* N^2}\frac{\partial \rho_o}{\partial y}\right) + \left(\frac{g}{\rho_* N^2}\frac{\partial \rho_o}{\partial y}\right)\frac{\partial}{\partial z}\right]v + \frac{\partial}{\partial z}\left[\frac{-1}{\rho_* N^2}\left(\frac{\partial}{\partial t} + U_o\frac{\partial}{\partial x}\right)\frac{\partial}{\partial z}\right]p = 0, \quad (14)$$

where

$$N^2(z) = -\frac{g}{\rho_*}\frac{\partial \rho_1}{\partial z} \quad (15)$$

represents the buoyancy frequency (see appendix A).

b. *Single-mode projection onto the vertical eigenfunctions*

The vertical dependencies of the state variables in (12)–(14) are projected onto the orthogonal set of eigenfunctions $\psi_n(z)$ defined in appendix A:

$$u = \sum_n u_n(x, y, t)\psi_n(z), \quad (16)$$

$$v = \sum_n v_n(x, y, t)\psi_n(z), \quad \text{and} \quad (17)$$

$$p = \sum_n p_n(x, y, t)\psi_n(z). \quad (18)$$

The single-mode projection can be obtained by truncating the sums in (16)–(18) at $n = 1$, substituting into (12)–(14), multiplying each equation by ψ_1, integrating vertically, and applying the boundary conditions (A2). In this single-mode model, the terms projected onto vertical modes greater than 1 are simply neglected.

For zonally propagating wave solutions, the x–t dependencies of the coefficients u_1, v_1, and p_1 in the expansions (16)–(18) are assumed to have the form $e^{i(kx-\omega t)}$. The resulting system of equations can then be written in matrix form as

$$\begin{bmatrix} \overline{U^{(1)}}k & i\{\beta y - (\overline{U_y^{(1)}} + \overline{f^*})\} & \left(\frac{1}{\rho_*} - \overline{\alpha}\right)k \\ -i\beta y & \overline{U^{(1)}}k & -\frac{i}{\rho_*}\frac{\partial}{\partial y} \\ c_1^2\rho_* k & -i\rho_*\left\{g(\overline{H_y^{(1)}} + \overline{H_y^{(2)}}) + c_1^2\frac{\partial}{\partial y}\right\} & (\overline{U^{(1)}} + \overline{U^{(2)}})k \end{bmatrix}\begin{bmatrix} u_1 \\ v_1 \\ p_1 \end{bmatrix} = \omega\begin{bmatrix} 1 & 0 & \frac{1}{c_1^2\rho_*}\overline{U^{(2)}} \\ 0 & 1 & 0 \\ 0 & 0 & 1 \end{bmatrix}\begin{bmatrix} u_1 \\ v_1 \\ p_1 \end{bmatrix}, \quad (19)$$

where u_1, v_1, and p_1 are now functions only of y. The mean-field coefficients in (19) are

$$\overline{U^{(1)}}(y) \equiv \int_{-H}^{0} U_o\psi_1\psi_1\, dz, \quad (20)$$

$$\overline{U_y^{(1)}}(y) \equiv \int_{-H}^{0} \frac{\partial U_o}{\partial y}\psi_1\psi_1\, dz, \quad (21)$$

$$\overline{U^{(2)}}(y) \equiv \int_{-H}^{0} \frac{-c_1^2}{N^2}\frac{\partial U_o}{\partial z}\frac{\partial \psi_1}{\partial z}\psi_1\, dz, \quad (22)$$

$$\overline{f^*}(y) \equiv \int_{-H}^{0} \frac{g}{\rho_* N^2} \frac{\partial U_o}{\partial z} \frac{\partial \rho_o}{\partial y} \psi_1 \psi_1 \, dz$$

$$= \int_{-H}^{0} \frac{\beta y}{N^2} \frac{\partial U_o}{\partial z} \psi_1 \psi_1 \, dz, \tag{23}$$

$$\overline{\alpha}(y) \equiv \int_{-H}^{0} \frac{U_o}{\rho_* N^2} \frac{\partial U_o}{\partial z} \frac{\partial \psi_1}{\partial z} \psi_1 \, dz, \tag{24}$$

$$\overline{H_y^{(1)}}(y) \equiv c_1^2 \int_{-H}^{0} \frac{1}{\rho_*} \frac{\partial}{\partial z} \left(\frac{1}{N^2} \frac{\partial \rho_o}{\partial y} \right) \psi_1 \psi_1 \, dz, \tag{25}$$

and

$$\overline{H_y^{(2)}}(y) \equiv c_1^2 \int_{-H}^{0} \frac{1}{\rho_*} \left(\frac{1}{N^2} \frac{\partial \rho_o}{\partial y} \right) \frac{\partial \psi_1}{\partial z} \psi_1 \, dz. \tag{26}$$

The relative magnitudes of the coefficients in (19) can be computed from time-averaged zonal POCM

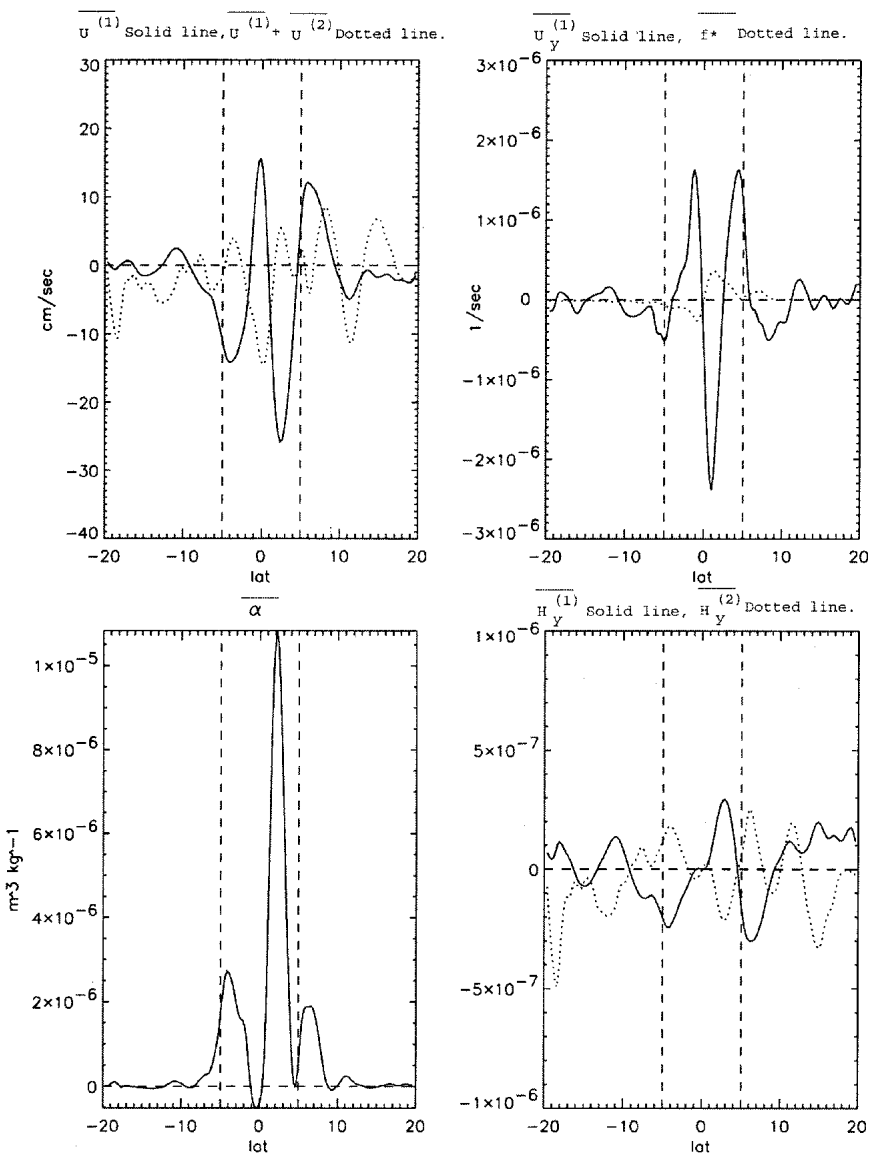

FIG. 6. Plots of the mean fields from (20)–(26) computed over the period from 8 Jul to 6 Sep 1995 from the mean zonal current section along 134°W (shown in Fig. 3). (top left) A plot of $\overline{U^{(1)}}$ (solid line) and $\overline{U^{(2)}} + \overline{U^{(1)}}$ (dotted line). (top right) A plot of $\overline{U_y^{(1)}}$ (solid line) and $\overline{f^*}$ (dotted line). (bottom left) A plot of $\overline{\alpha}$; (bottom right) a plot of $\overline{H_y^{(1)}}$ (solid line) and $\overline{H_y^{(2)}}$ (dotted line).

model output (Fig. 6). In the region of dispersion space where TIWs are found (see Fig. 8e),

$$|\omega/k| \leq 1 \text{ m s}^{-1}, \tag{27}$$

in which case it is apparent that

$$|\overline{\alpha}| \ll \left|\frac{1}{\rho_*}\right| \quad \text{and} \tag{28}$$

$$\left|\frac{\omega}{k}\frac{1}{c_1^2\rho_*}\overline{U^{(2)}}\right| \ll \left|\frac{1}{\rho_*}\right|. \tag{29}$$

If these smaller terms are neglected, (19) reduces to

$$\begin{bmatrix} \overline{U^{(1)}}k & i\{\beta y - (\overline{U_y^{(1)}} + \overline{f^*})\} & \frac{1}{\rho_*}k \\ -i\beta y & \overline{U^{(1)}}k & -\frac{i}{\rho_*}\frac{\partial}{\partial y} \\ c_1^2\rho_* k & -i\rho_*\left\{g(\overline{H_y^{(1)}} + \overline{H_y^{(2)}}) + c_1^2\frac{\partial}{\partial y}\right\} & (\overline{U^{(1)}} + \overline{U^{(2)}})k \end{bmatrix} \begin{bmatrix} u_1 \\ v_1 \\ p_1 \end{bmatrix} = \omega \begin{bmatrix} u_1 \\ v_1 \\ p_1 \end{bmatrix}. \tag{30}$$

Equation (30) bears a striking resemblance to the matrix equation for a two-layer, reduced-gravity model [see (B1) in appendix B]. For the case of zero mean flow, the matrix equations are exactly the same. When the mean background fields are considered, counterparts can be identified in the two equations (see Table 1). The equivalent to $g'H(y)$ in (B1) becomes c_1^2 in (30); U_o becomes $\overline{U^{(1)}}$ in the equations for u_1 and v_1; U_o becomes $\overline{U^{(1)}} + \overline{U^{(2)}}$ in the equation for pressure where the addition of $\overline{U^{(2)}}$ is an effect of the chain rule; $\partial U_o/\partial y$ is modified to $\overline{U_y^{(1)}} + \overline{f^*}$; and $\partial H(y)/\partial y$ becomes $\overline{H_y^{(1)}} + \overline{H_y^{(2)}}$. Gradients in mean layer thickness, $\partial H/\partial y$ in the two-layer, reduced-gravity model, are represented by $\overline{H_y^{(1)}} + \overline{H_y^{(2)}}$ in the projection model; $\overline{H_y^{(1)}}$ corresponds to the geostrophic pressure gradient in the two-layer, reduced-gravity model, while $\overline{H_y^{(2)}}$ is a new term in the projection model, which resembles a density gradient in geostrophic balance with $\overline{U^{(2)}}$. The term f^* in the projection model is analogous to βy divided by the gradient Richardson number, $N^2/(\partial U_o/\partial z)^2$ in the two-layer, reduced-gravity model.

Energy conversions in the single-mode projection model are defined by the following equation:

$$-\rho_*(\overline{U_y^{(1)}} + \overline{f^*})[v_1u_1] - \frac{g}{c_1^2}(\overline{H_y^{(1)}} + \overline{H_y^{(2)}})[v_1p_1] - [(v_1p_1)_y] = \omega_i[E_1], \tag{31}$$

TABLE 1. A summary of the relationship between the terms in the two-layer, reduced-gravity model and the single-mode projection model.

Reduced-gravity model	Projection model momentum equations	Projection model continuity equation
$g'H(y)$	$\overline{U^{(1)}}$	c_1^2
$U_o(y)$	$\overline{U_y^{(1)}} + \overline{f^*}$	$(\overline{U^{(1)}} + \overline{U^{(2)}})$
$\partial U_o/\partial y$		
$\partial H/\partial y$		$(\overline{H_y^{(1)}} + \overline{H_y^{(2)}})$

where ω_i is the imaginary part of the eigenvalue; $E_1 = \rho_*(v_1^2 + u_1^2) + p_1^2/(\rho_* c_1^2)$ is the total vertically integrated mode-1 perturbation energy; $p_1^2/(\rho_* c_1^2)$ is the potential energy, which has been derived from the traditional definition (Luther and Johnson 1990); and the bracketed terms have been zonally averaged over a wavelength. From left to right, the terms in (31) represent 1) barotropic, 2) Kelvin–Helmholtz and 3) baroclinic energy conversions, and 4) wave flux divergence, which only redistributes energy in the domain. The $(\partial U_o/\partial z)w$ term in (3) is the source of Kelvin–Helmholtz energy conversions. In matrix (30), $(\partial U_o/\partial z)w$ is represented by $\overline{f^*}$, $\overline{\alpha}$, and $\overline{U^{(2)}}/(c_1^2\rho_*)$ in the first-row equation. For the particular scales considered here, $\overline{\alpha}$ and $\overline{U^{(2)}}/(c_1^2\rho_*)$ are negligible, as previously noted from (28) and (29), while $\overline{f^*}$ can make a small contribution to Kelvin–Helmholtz energy conversions near the equator.

The system of equations in (30) avoids arbitrary depth averaging and contains information about the variability of vertical mode-1 structure of the ocean. Though still limited to only one degree of freedom in the vertical structure, this projection model provides a less subjective and more representative model of a single-vertical-mode equatorial ocean than the two-layer, reduced-gravity model while retaining relatively simple physics (Flierl 1978). The model can easily be extended to more complex vertical structure simply by including higher-order vertical modes (see section 3c).

The matrix (30) is a set of linear differential equations in y, which for a given k was solved on a 1/4° staggered grid with u_1 and v_1 sharing the same grid points and with p_1 at the adjacent grid points. The northern and southern boundaries were placed at the u_1 and v_1 grid points at 19.75°N and 19.75°S. The eigenvalues and eigenfunctions of the matrix were solved using the EISPACK linear algebra package.

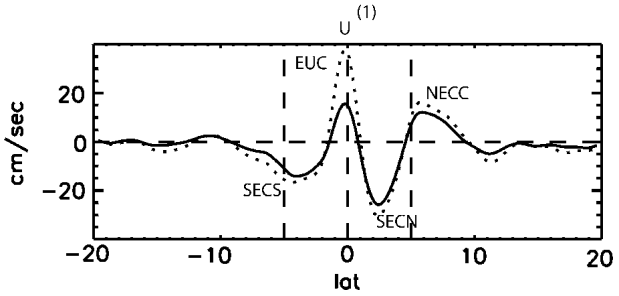

FIG. 7. Two different estimates of the upper-ocean mean velocity along 134°W. Both are derived from the mean vertical velocity section shown in Fig. 3. The solid line is $\overline{U^{(1)}}(y)$ from the single-mode projection model. The dotted line is a 260-m vertical average of the $U(y, z)$ section in Fig. 3.

c. Projection onto higher-order modes

The matrix (30) can be expanded to include higher-order vertical modes. The method is similar to that described for one mode in section 3b. As before, the state variables in (12)–(14) are expanded in terms of the orthogonal set of vertical eigenfunctions $\psi_i(z)$ according to (16)–(18) and the sums are truncated at $i = J$. The set of equations for mode j, $j = 1, \ldots, J$, is obtained by multiplying the resulting equation by ψ_j and vertically integrating (Lyman 2002).

4. Application of the projection model

The meridional structure and dispersion characteristics of solutions to the linear projection model are examined here by substituting the mean current profile from POCM (Fig. 3) into the eigenvalue problem (30). The characteristics of the SSH variability from the eigenvectors of the projection model are compared with those from the wavelet analysis of POCM SSH over the same time period presented in section 2. The single-mode projection model is considered in section 4a. The effects of higher-order vertical modes are investigated in sections 4b and 4c.

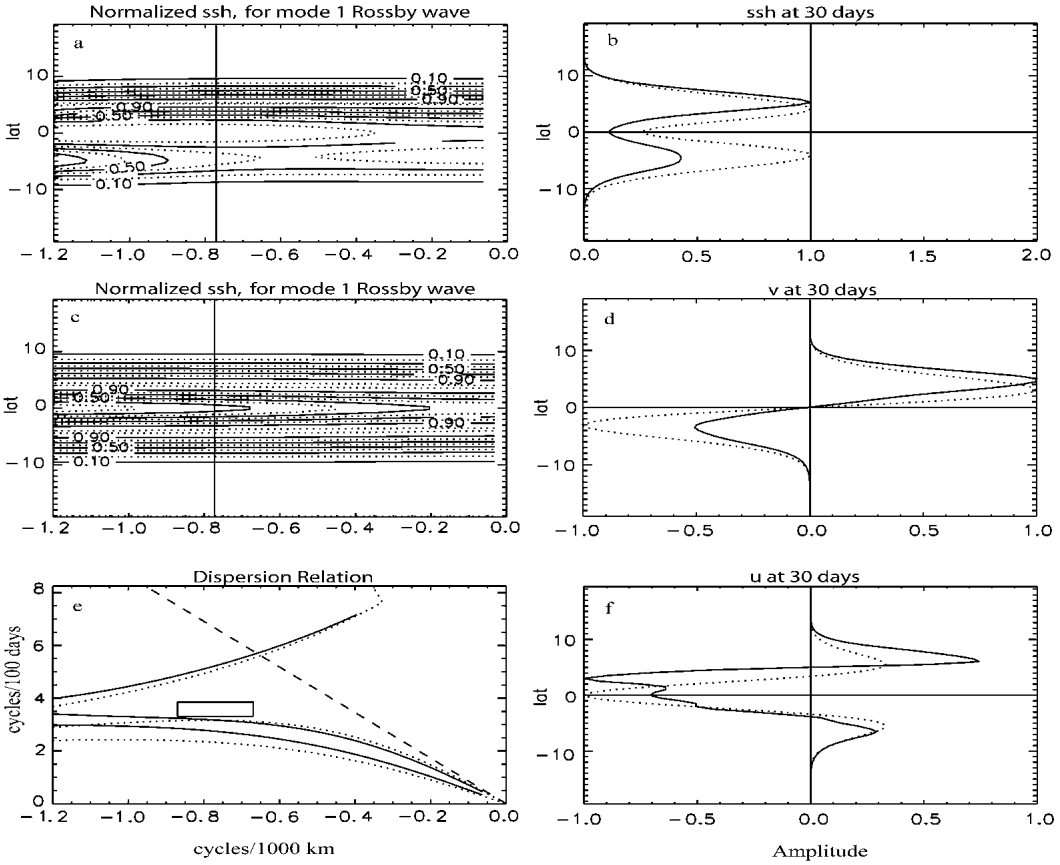

FIG. 8. The solutions to the single-mode projection model. (a) A contour plot of SSH of the $n = 1, m = 1$ Rossby wave vs wavenumber for the case with the mean flow $\overline{U^{(1)}}(y)$ shown in Fig. 7. (b) A latitudinal profile of the eigenfunction for SSH for the 1300-km, 30-day wave, with solid and dotted lines representing the eigenfunctions for the mean flow and zero mean flow cases, respectively. (c) Same as (a), but for the case of zero mean flow. (d) and (f) Same as (b) but for the eigenfunctions of v and u, respectively. (e) The dispersion relation, with the solid lines for the eigenvalues from the mean flow case and the dotted lines for the eigenvalues from the zero mean flow case. The black dashed line represents a phase speed of 1 m s^{-1}. The black box represents an estimate of the wavenumber–frequency content of TIWs from spectral analysis of the SSH fields from POCM.

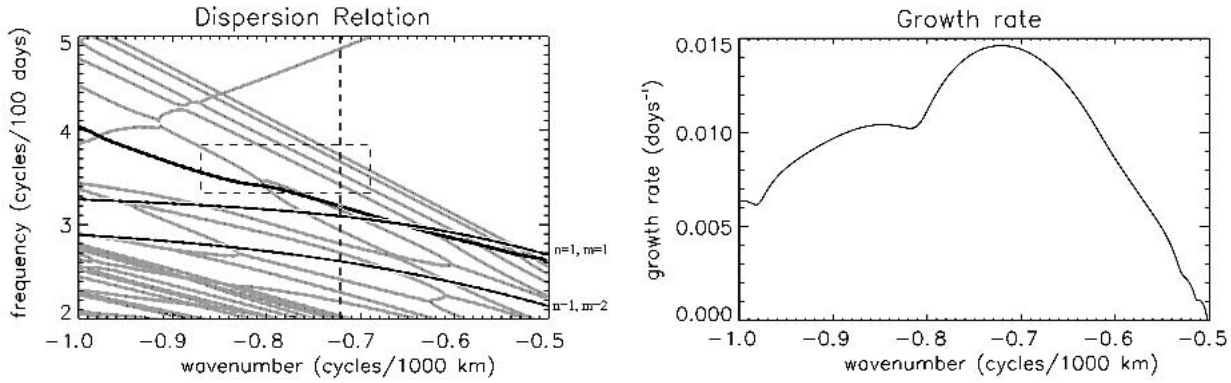

FIG. 9. The eigenvalues from the stability analysis of the two-mode projection model. (left) The wavenumber–frequency distribution. The fastest-growing mode is a thick black line; all other solutions are gray. The fastest-growing solution marked by a black and white diamond at a wavenumber of -0.72 cycles (1000 km)$^{-1}$ (corresponding to a wavelength of 1384 km) is plotted in Fig. 11. The thin black lines are the stable solutions of the single-mode projection model, with mode numbers labeled along the right axis. The dashed box in the plot represents the estimate of the wavenumber–frequency content of TIWs from spectral analysis of SSH fields from POCM. (right) The growth rate for the thick black line in the left panel.

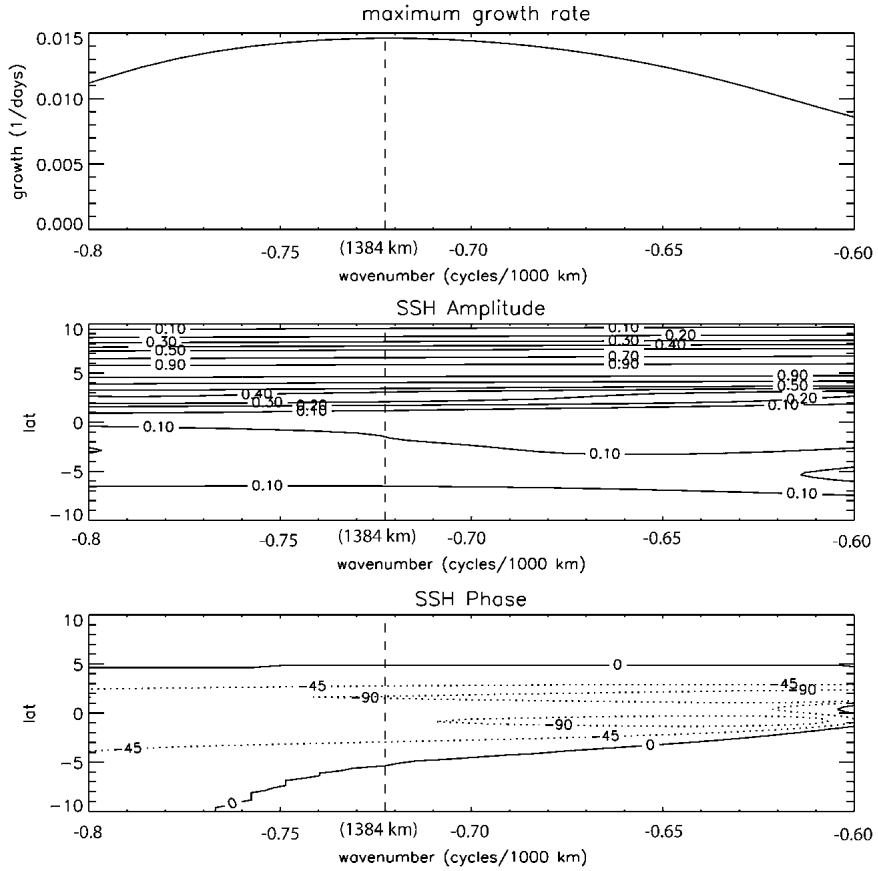

FIG. 10. The eigenvalues and eigenvectors from the stability analysis of the two-mode projection model. (top) The growth rate of the solutions as a function of wavenumber. The fastest-growing solution at a wavelength of 1384 km is marked by a dashed line, and the associated eigenvector is plotted in Fig. 11. Contour plots of the (middle) amplitude and (bottom) phase of the SSH eigenfunctions as a function of wavenumber.

For each application of the projection model, the dispersion relation is obtained by computing the eigenvalues at closely spaced values of the zonal wavenumber, k. The real and imaginary parts of the eigenvalue, ω, for each k represent, respectively, the frequency and the growth rate of the wave. The phase relationships among u, p, and v can be used to obtain the energy transfers between the mean and the perturbations. If the wave is stable, u and p are both in quadrature with v, the conversion terms in (31) vanish, and there is no energy transfer.

a. Single-mode projection

It was shown in section 3b that the structure of the equations for the simple, single-mode projection model are similar to those of the two-layer, reduced-gravity model. The single-mode projection provides a good first-order look at the effects of mean fields on the structure and dispersion characteristics of TIWs.

The mean background current in POCM (Fig. 3) was adjusted slightly for the computation of mean fields in (20)–(26) to represent more closely the geostrophic currents in the model by reducing the effects of near-surface Ekman currents. This was achieved by replacing the mean current in the top layer of the POCM model with the mean current in the second layer of the model.

Figure 7 shows the meridional structure of $\overline{U^{(1)}}(y)$, which is analogous to the upper-layer mean zonal velocity $U(y)$ of a two-layer, reduced-gravity model (see Table 1). The presence of the NECC, SECN, EUC, and SECS are apparent in Fig. 7. The projection thus retains the major features of the mean currents that may be important to the stability of the equatorial current system.

For the purposes of the two-layer, reduced-gravity model $U(y)$ was taken to be the average over the upper 260 m of the POCM model, and it is shown as the

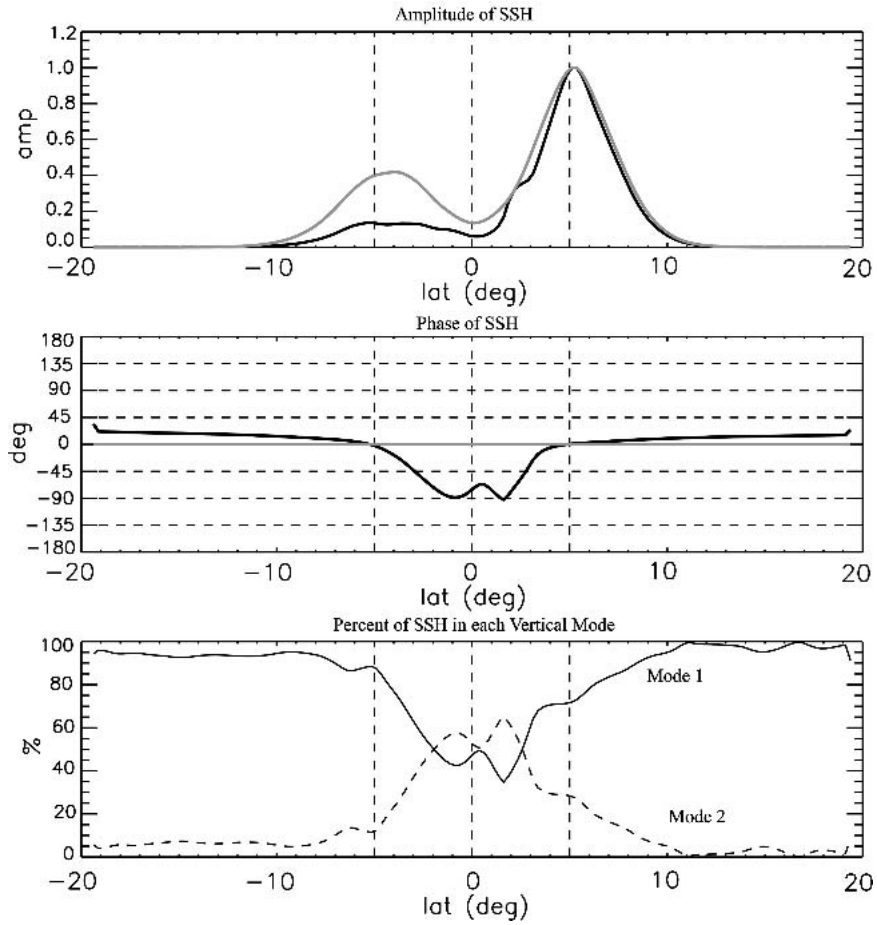

FIG. 11. Latitudinal profiles of the (top) amplitude and (middle) phase relative to 5°N for the eigenfunctions of SSH of the fastest-growing solution in the two-mode projection model (black lines) and the solutions from the single-mode projection model with the same wavenumber (gray lines). (bottom) The percent of SSH in each vertical mode, with the solid line representing mode 1 and the dashed line representing mode 2. This solution has an e-folding time of 68 days, a period of 31 days, and a wavelength of 1384 km.

dotted line in Fig. 7. The amplitudes of the main features of the equatorial current system in $\overline{U^{(1)}}(y)$ are diminished when compared with $U(y)$. The amplitude of $U(y)$ is sensitive to the depth of the vertical average, emphasizing its arbitrary nature (section 3). The differences between in $\overline{U^{(1)}}(y)$ and $U(y)$ in the westward currents (the SECN and SECS), which Philander (1976) found to be less stable than the eastward currents, are relatively small. The largest difference is in the relatively stable eastward EUC whose vertical structure contains higher vertical modes than the NECC, SECN, and SECS (see Fig. 3) and is therefore incompletely represented by the single-mode projection model. The importance of the more complex vertical structure of the EUC is investigated in sections 4b and 4c, using the projection models with two and five vertical modes.

The eigenmodes for the Yanai and first two meridional-mode Rossby waves were computed using the single-mode projection model and the POCM mean fields (Fig. 8). The first-meridional-mode ($m=1$) Rossby waves are closest in dispersion space to the observed SSH variability in POCM (Fig. 8). Eigensolutions for the case with no background flow are shown by the dotted lines in Fig. 8. The mean flow systematically reduces the phase speed of $m = 1$ Rossby waves for wavenumbers smaller than 0.75 cycles (1000 km)$^{-1}$ (Fig. 8e). In contrast, the mean flow increases the phase speeds of the second-meridional-mode ($m = 2$) Rossby waves at all wavelengths. All of the solutions are effectively stable in this single-mode projection; that is, the most unstable solutions have *e*-folding times several times longer than the ~9-month duration of the TIW season.

While the dispersion characteristics in the single-mode projection model are only moderately affected by the background mean currents, the meridional structure of the $m = 1$ Rossby wave is significantly altered, as shown in Figs. 8d–f for solutions with 30-day period and 1300-km wavelength. The solid lines represent the solutions based on $\overline{U^{(1)}}(y)$ shown in Fig. 7, while the dash–dotted lines represent the solutions for the zero mean flow case. For SSH (Fig. 8d), the mean flow causes the maxima to shift poleward, the amplitude in the south to decrease to 40% of the amplitude in the north, and the trough at the equator to deepen by 50%. The structures in u and v show similar differences, with peaks shifting poleward and amplitudes decreasing in the south. As noted above, these solutions are stable;

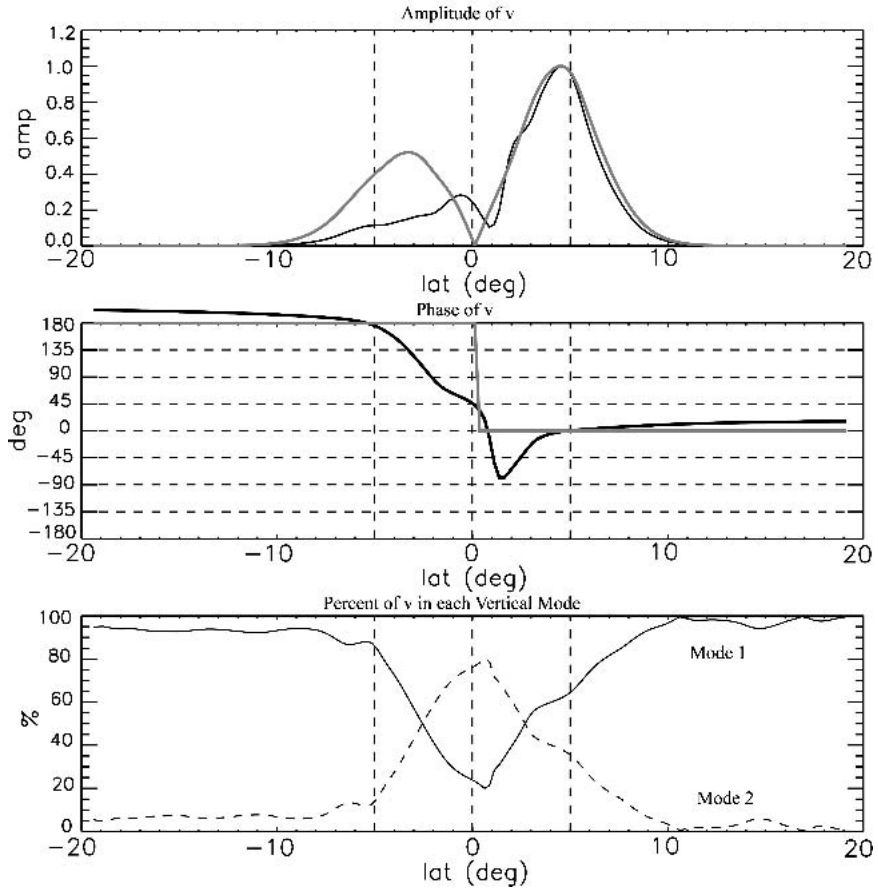

FIG. 12. The same as Fig. 11, but for the eigenfunction of v.

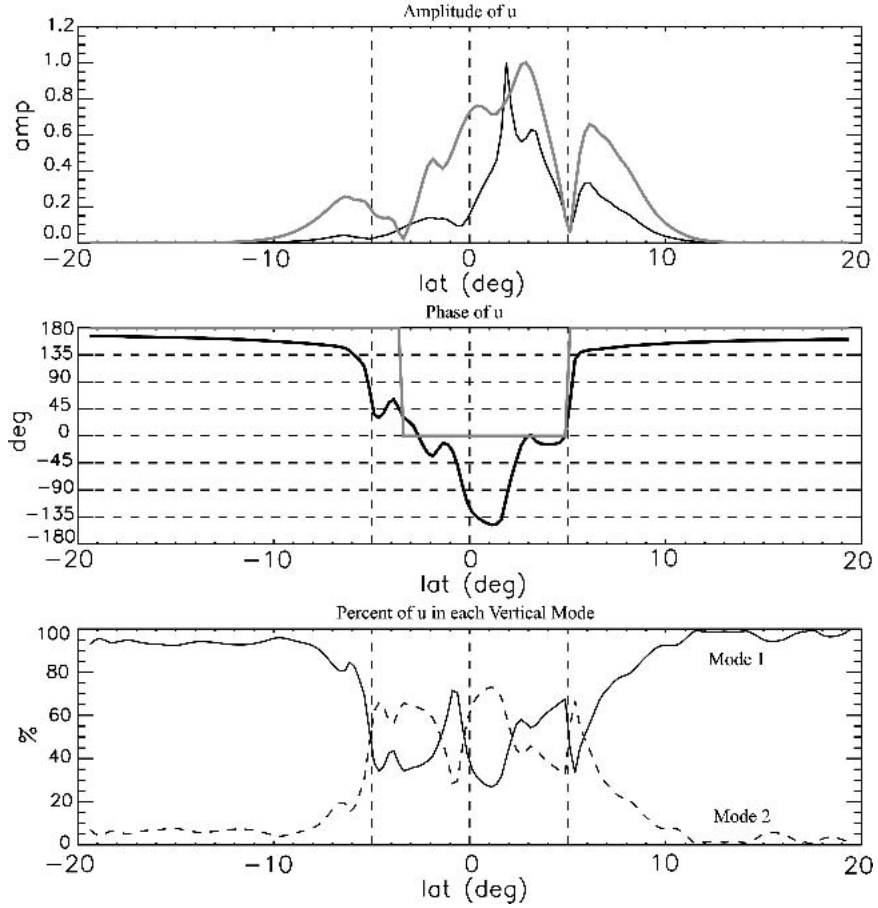

FIG. 13. The same as Fig. 11, but for the eigenfunction of u.

hence u and p are in or out of phase with each other at all latitudes and in quadrature with v.

These effects of the mean currents on the meridional structure of the solutions are a robust feature of this analysis. At all wavenumbers, the mean flow deepens the trough in p (SSH) at the equator and shifts the northern maximum poleward (Fig. 8a). While the zero mean flow case shows symmetric structure in amplitude for all wavenumbers (Fig. 8c), the presence of the mean flow can be seen to decrease the amplitude of p in the

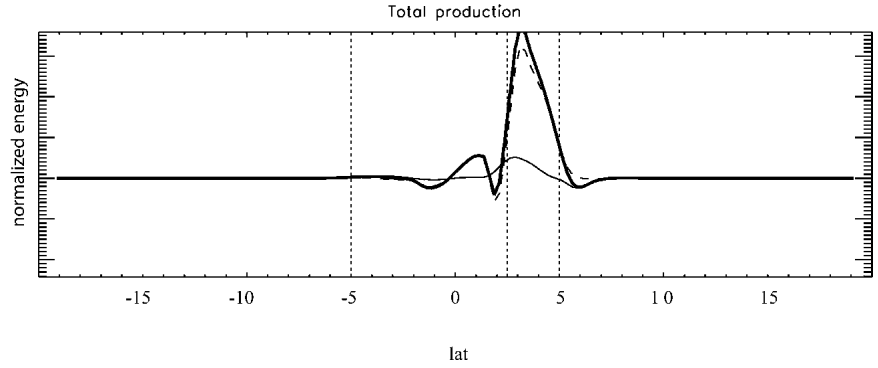

FIG. 14. The energy conversion from the two-mode projection model for the mean flow $\overline{U^{(1)}}(y)$ shown in Fig. 7. The thick solid line represents the total energy conversion. The thin solid line represents the baroclinic conversion and the dashed line represents the barotopic conversion [see (31)]. The vertical dotted lines mark 5°S, 5°N, and the latitude of the core of the SECN.

south for the full range of 800–20 000-km wavelengths shown. At the highest wavenumbers, the amplitude at 5°S is 60% of that at 5°N. As the wavenumber decreases, the amplitude in the south also decreases, with the ratio reaching a minimum of 0.35 at a wavenumber of -0.55 cycles (1000 km)$^{-1}$, corresponding to a wavelength of about 1800 km. The observed 1000–2000-km wavelengths of TIWs fall in the region where the meridional asymmetry in SSH is most sensitive to changes in wavenumber.

Because the single-mode projection model is stable for the mean zonal velocity section considered here, these solutions cannot explain the phase structure of TIWs in POCM. However, the meridional structures of the amplitudes of the wave solutions close to the TIW period and wavenumber range obtained from the single-mode projection model are similar to those deduced in section 2b from POCM SSH fields.

b. Two-mode projection

By increasing the vertical resolution to include the first two vertical modes, the mean current structure is more completely represented. The added complexity produces a set of six coupled equations (Lyman 2002). The mean fields from the two-mode projection model are computed over the same time period as for the single-mode projection model.

Unlike the single-mode projection model, the two-mode projection model produces unstable solutions (Fig. 9). The fastest-growing solution has a wavelength of 1384 km. The dispersion relation for the two-mode projection model shows an increase in phase speed when compared with the single-mode model in this wavelength range. The observed wavenumber–frequency characteristics of the TIWs in POCM (dashed box in Fig. 9) are in slightly better agreement with the dispersion relation of the two-mode projection model. At smaller wavenumbers, the solutions become stable, splitting into two stable modes at $k = -0.5$ cycles (1000 km)$^{-1}$. The characteristics of these two stable modes are examined in section 5.

As in the case of the single-mode projection model, the meridional structures of the eigensolutions of the two-mode projection model are sensitive to wavenum-

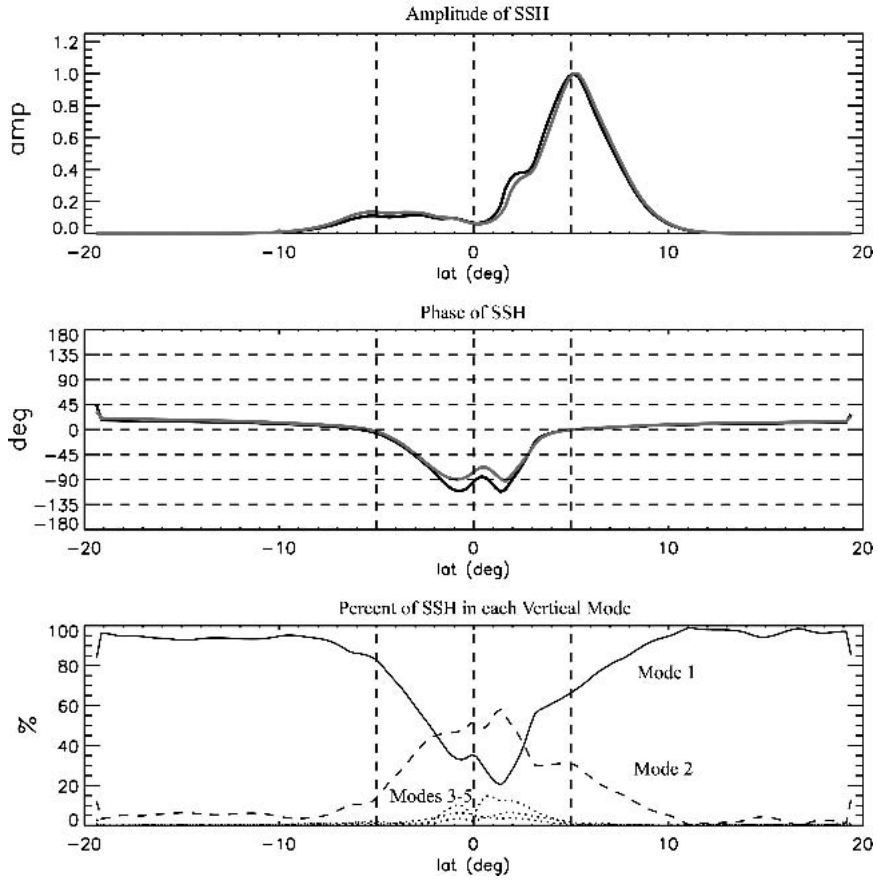

FIG. 15. The same as Fig. 11, except the black lines are the eigenfunction of SSH for the fastest-growing solution in the five-mode projection model. This solution has an *e*-folding time of 73 days, a period of 32 days, and a wavelength of 1592 km. The gray lines in the top two panels are the solution for the two-mode projection model in Fig. 11.

ber in the TIW wavenumber range. For the fastest-growing solution over the TIW wavenumber range, amplitudes at 5°N are 2–10 times those at 5°S and the phase at 5° north leads the phase at 5°S by 0°–45° (Fig. 10). This sensitivity provides an environment in which a wide range of meridional structures is possible, depending on the wavenumber, posing challenges to quantitative association of the observed structures in the SSH record with specific eigensolutions.

The amplitude structure in SSH for the fastest-growing mode from the two-mode projection model is similar to that of the stable solution from the single-mode projection model (Fig. 11). The peaks in SSH amplitude are still at 5°N and 5°S, with a larger amplitude in the north. An important distinction is that the amplitude in the north is more than 5 times that in the south, as compared with less than a factor of 3 difference in the single-mode projection model at this wavelength of 1384 km. This structure of SSH from the two-mode projection model is more consistent with the SSH variability in POCM during the early stages of the 1995/96 TIW season (Fig. 5).

Whereas the stable single-mode solution had constant phase with latitude, the phase of the unstable two-mode solution varies with latitude (Fig. 11). For this 1384-km wavelength, SSH at 5°S is in phase with SSH at 5°N. The approximate 90° phase lag near the equator is evidence of an equatorward eddy transport of zonal momentum, which leads to the barotropic conversion of energy in the presence of the large mean velocity shears in the region. As in amplitude, these latitudinal variations of the phase are similar to latitudinal "tipping" of the structures of SSH in POCM (Fig. 5).

The vertical structure of the state variables is also different from the single-mode projection model. Except within a few degrees of the equator, SSH variability is dominated by the first baroclinic mode (Fig. 11). Near the equator, the variability is approximately equally partitioned between vertical modes 1 and 2. The meridional velocity v has a vertical structure similar to SSH poleward of 2°. Unlike SSH, however, v is almost wholly made up of mode 2 near the equator (Fig. 12). Within 5° of the equator, u alternates between being dominated by modes 1 and 2 (Fig. 13). Outside of this region, u variability is dominated by mode 1, similar to SSH and v.

The relationships between p, u, and v in the two-mode projection are not as simple as in the single-mode projection. With the onset of instability, the phases of u and p are no longer in quadrature with v (Figs. 11, 12, and 13), and there is a transfer of energy between the mean and the perturbations in accord with (31). The energy transfer of this mode is mostly barotropic (Fig. 14) and occurs between about 2.5° and 4°N on the poleward flank of the SECN (Fig. 7). Baroclinic energy conversion is not negligible (Fig. 14), however, also contributing to perturbation energy conversion on the poleward flank of the SECN. The dominance of the poleward flank of the SECN as a region of energy transfer hints at its importance in the development of the instability.

The nature and location of the maximum energy transfer are not surprising. Previous linear stability analyses have all found barotropic conversion associated with the SECN to be the primary source of energy for TIWs (Philander 1978; Proehl 1998). However, there has been debate as to which side of the SECN is important. Originally, Philander (1978) and Cox (1980) found the shear between the SEC and the NECC to be the most important, which has been supported by observations (Baturin and Niiler 1997; Kennan 1997). A more recent linear stability analysis by Proehl (1998) finds that the shear between the SECN and the EUC is the energy source for the instabilities, a region where observations have also found barotropic energy transfer (Hansen and Paul 1984; Luther and Johnson 1990; Qiao and Weisberg 1995). The present analysis finds that the shear on the poleward flank of SECN near the maximum of the SECN is the location of most of the energy transfer. Because this region of energy transfer

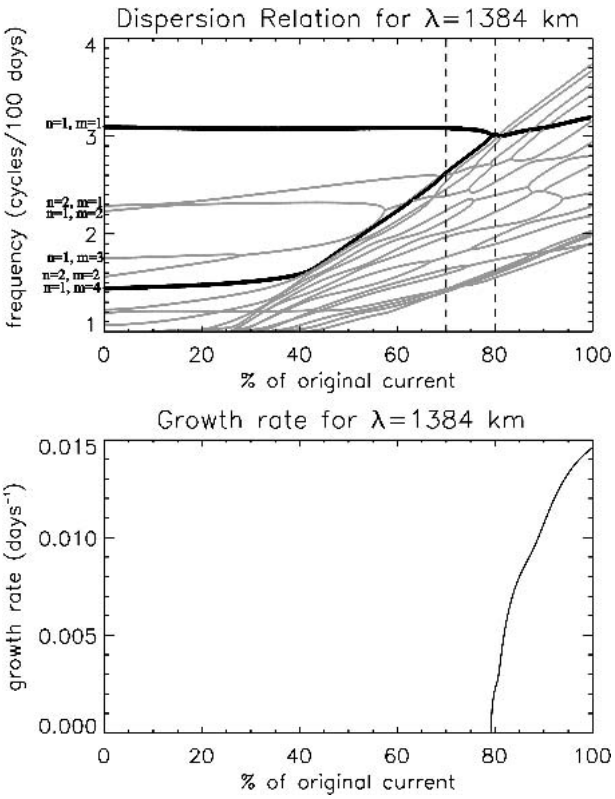

FIG. 16. The eigenvalues from the stability analysis of the two-mode projection model for a range of mean currents with a wavelength of 1384 km. (top) The frequency plotted as a function of percentage of $\overline{U}(y, z)$ at 134°W. The fastest-growing mode is a thick black line. The evolution of the solutions that start off as $n = 1$, $m = 1$ and the $n = 1$, $m = 4$ Rossby waves in an ocean at rest are marked as black lines. All other solutions are gray. (bottom) The growth rate for the thick black line in the top panel.

is far from the NECC, the present analysis suggests that the NECC is not crucial to the instability.

c. Five-mode projection

In the area of wavenumber–frequency space in which we are interested, it was shown in section 4a that the single-mode projection produced stable solutions while the two-mode projection model in section 4b was able to produce instabilities that are similar to the initial stages of the 1995/96 TIW season in POCM. It is of interest to determine whether projection onto additional higher-order vertical modes changes the characteristics of the instability. This was investigated by increasing the vertical resolution of the model to include projection onto the first five baroclinic modes. The mean fields for the five-mode projection model were computed over the same time period as the single- and two-mode projection models considered previously.

For the fastest-growing solution (Fig. 15), there are minor changes from the two-mode projection: the *e*-folding time increases from 68 to 73 days and the wavelength increases from 1384 to 1592 km. The latitudinal structures of the eigenvectors are almost identical. The amplitudes in the top panel are essentially identical at all latitudes; the phases differ near the equator by only about 10°. The five-mode solution is almost wholly made up of the first two baroclinic modes, with higher-order modes cumulatively accounting for less than 25% of the variability near the equator.

We conclude that there is little difference in the meridional structure, vertical structure, or dispersion characteristics between the fastest-growing solutions in the two- and five-mode projections. The important physics are evidently captured in the two-mode projection. The analysis in section 5 therefore focuses on the simpler and more computationally efficient two-mode projection.

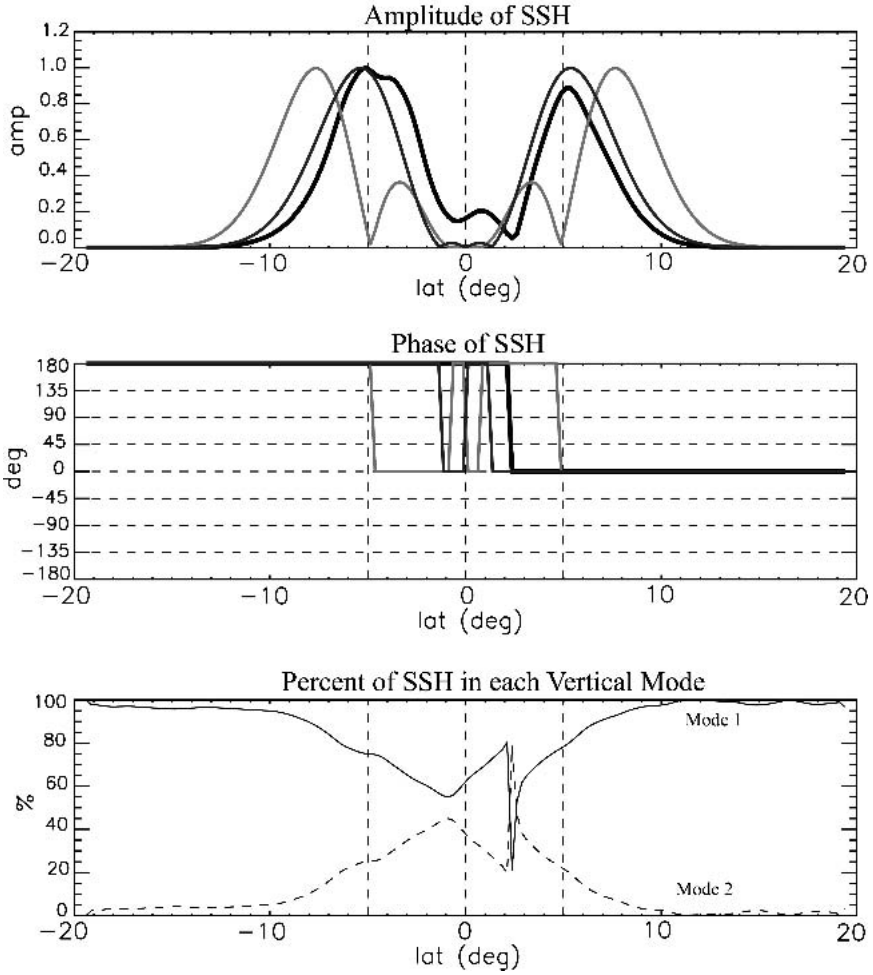

FIG. 17. Same as Fig. 11, except the black lines are from the lower black line in Fig. 16 at 70% of $\overline{U}(y, z)$. The dark gray lines are from the $n = 1$, $m = 2$ Rossby wave at 0% of $\overline{U}(y, z)$ in Fig. 17, and the light gray lines are from the $n = 1$, $m = 4$ Rossby wave at 0% of $\overline{U}(y, z)$ in Fig. 16.

5. Resonance

The solutions obtained from the two-mode projection model were shown to be unstable over a range of wavenumbers (Fig. 9). In this section, the bifurcation of free equatorial trapped Rossby waves into unstable waves is investigated by considering a sequence of model runs in which the background zonal currents are successively increased from a state of rest. The two-mode projection model was run 1000 times for the wavelength of 1384 km, the fastest-growing solution in Fig. 9 for the background mean current $\overline{U}(y, z)$ in Fig. 3. In each successive run, $j = 1, \ldots, 1000$, the base state was set to $0.001j\overline{U}(y, z)$. The results can be summarized in a bifurcation diagram that shows frequency and growth rate as a function of the strength of the basic flow (Fig. 16).

For mean flows less than 80% of $\overline{U}(y, z)$, the first-vertical- ($n = 1$), first-meridional (m=1)-mode Rossby wave at this wavelength is essentially unaffected by the mean currents (Fig. 16). When the mean zonal current is about 80% of $\overline{U}(y, z)$, the frequencies of the $n = 1$, $m = 1$ Rossby wave and a higher-order Rossby wave coincide at 0.03 cpd. For larger mean flows, the two eigenvalues are complex conjugates of each other, both having the same frequency (real part), one corresponding to exponential growth, the other to exponential decay. This demonstrates that the resonance that occurs when these two Rossby waves share the same frequency is responsible for TIW growth.

The higher-order Rossby wave that resonates with the $n = 1$, $m = 1$ Rossby wave to form TIWs does not have a clear classification in terms of free Rossby waves in a resting ocean. For zero mean flow, the Rossby wave that eventually resonates with the $n = 1$, $m = 1$ mode Rossby wave can be identified as the $n = 1$, $m = 4$ mode Rossby wave. As the mean zonal currents are increased from a resting ocean, the latitudinal structure of the higher-order Rossby wave changes as it shares the frequencies with lower-mode unstable waves. After the last of these interactions, when the current is increased to 70% of $\overline{U}(y, z)$, the higher-order Rossby wave has meridional structure in SSH that is more similar in phase and amplitude to the free $n = 1$, $m = 2$ Rossby wave than to the $n = 1, m = 4$ free Rossby wave from which the solution originated (Fig. 17). Classification of the higher-order Rossby wave is further complicated by its vertical structure (bottom panel of Fig. 17), which is dominated by the first baroclinic mode but also has a significant contribution from the second baroclinic mode near the equator.

The resonance between these two Rossby waves can also be examined as a function of increasing wavenumber for fixed mean current. When the mean zonal current is at 80% of $\overline{U}(y, z)$, the resonance between the two Rossby waves occurs at an approximate wavenumber and frequency of -0.71 cycles (1000 km)$^{-1}$ and 3 cycles (100 days)$^{-1}$, respectively (Fig. 18).

The upper branch of the fixed-current bifurcation follows the $n = 1$, $m = 1$ single-mode projection model Rossby wave and is easily identifiable as the $n = 1, m = 1$ Rossby wave. Its meridional SSH structure at -0.5 cycles (1000 km)$^{-1}$ is almost indistinguishable in phase and amplitude from the free mode solution from the single-mode projection model and its vertical structure is composed almost entirely of the first baroclinic mode (Fig. 19).

The lower branch is close to the single-mode projection model $n = 1$, $m = 2$ Rossby wave at low wavenumbers. As the wavenumber increases, however, the lower black curve in Fig. 18 steepens and approaches the upper branch. The meridional SSH structure of the lower branch at -0.5 cycles (1000 km)$^{-1}$ (Fig. 20) is very similar in phase and amplitude to the free mode solution from the single-mode projection model (gray lines in Fig. 20). Yet, near the equator its vertical structure has a significant contribution from the second baroclinic mode.

The above bifurcation analysis demonstrates that TIWs form from the resonance of two free Rossby waves in the two-mode projection model. When the mean background zonal current is slowly increased from rest, the phase speed of a higher-order Rossby wave increases to a point at which this wave eventually interacts with the $n = 1$, $m = 1$ Rossby wave. The

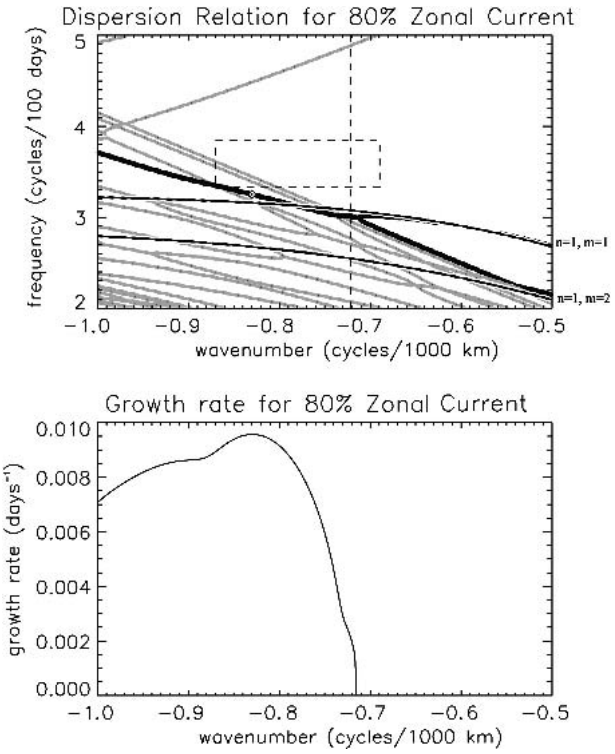

FIG. 18. The same as Fig. 9 but for a mean zonal current that is 80% of $\overline{U}(y, z)$ at 134°W. The fastest-growing solution is at -0.83 cycles (1000 km)$^{-1}$. The two stable Rossby waves that resonate to form the instability are marked as black lines in the top panel.

higher-order Rossby wave is an altered $n = 1$, $m = 2$ Rossby wave, with similar cross-equatorial amplitude and phase but a more complicated vertical structure than the free $n = 1$, $m = 2$ Rossby wave and can be traced back to the $n = 1$, $m = 4$ Rossby wave in a resting ocean.

6. Summary and conclusions

A linear stability analysis based on the mean zonal current along 134°W in POCM produced TIWs with cross-equatorial structures in SSH that resemble the filtered TIW SSH signal in POCM. The SSH amplitude at 5°N is 5 times that at 5°S and the phase "tips" westward with increasing distance from equator. This structure, is similar to that seen in TOPEX/Poseidon observations of SSH (CSLD). A bifurcation analysis in section 5 revealed that the model TIWs arise from the resonance of an altered $n = 1, m = 2$ Rossby wave with the $n = 1$, $m = 1$ Rossby wave.

TIWs have previously been investigated from numerous linear stability analyses of layer models. None of these previous models have been able to reproduce the observed latitudinal asymmetry of TIWs. For a given a mean current, these layer models have either low vertical resolution and an arbitrary vertical averaging scheme (Philander 1978; McCreary and Yu 1992) or high vertical resolution but limited depth range (Proehl 1998). The projection model presented in this paper avoids these problems by projecting the state variables onto the baroclinic eigenfunctions.

Perhaps surprisingly, two vertical modes were found to be sufficient to describe the initial stages of TIWs in POCM in the eastern equatorial Pacific Ocean. The addition of higher vertical modes (section 4c) resulted in TIWs with cross-equatorial structure, wavenumber–frequency content, and vertical structure very similar to the TIWs produced by the two-mode projection model. The single-mode projection model, however, was not able to produce an unstable solution in the wavenum-

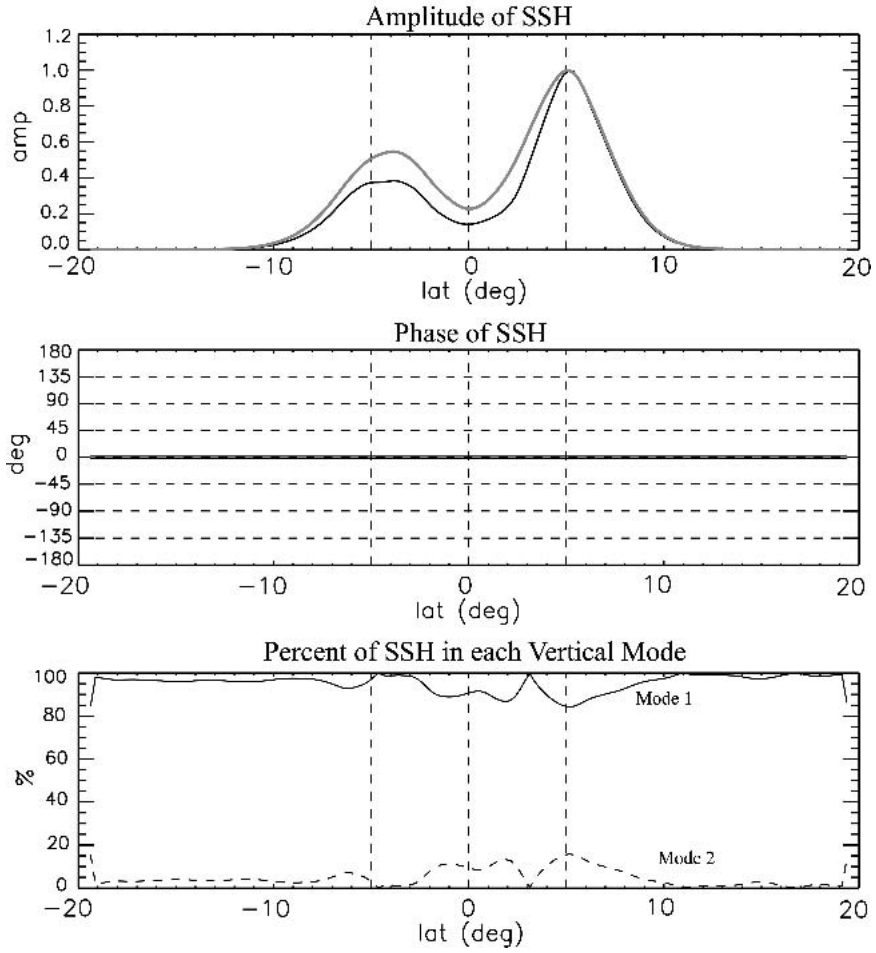

FIG. 19. The same as Fig. 11, except the thick lines are from the upper black curve in Fig. 18 at -0.5 cycles (1000 km)$^{-1}$ and the gray lines are from the $n = 1$, $m = 1$ Rossby wave single-mode projection model at -0.5 cycles (1000 km)$^{-1}$.

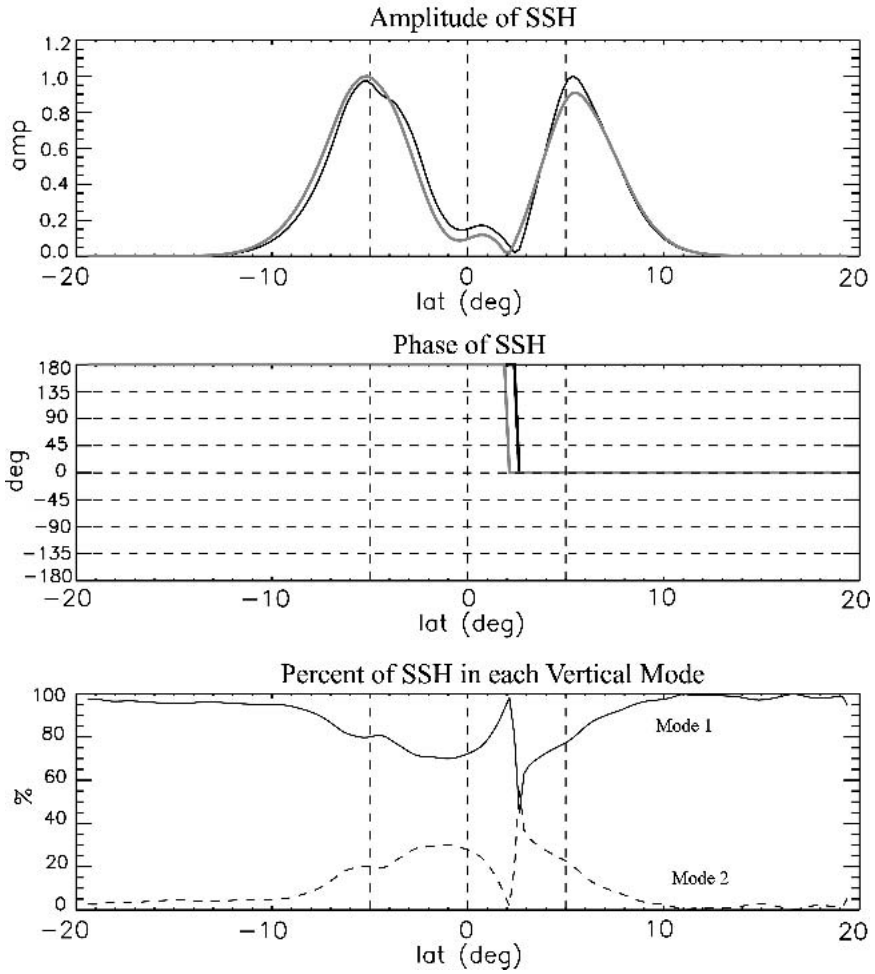

FIG. 20. The same as Fig. 11, except the thick lines are from lower black curve in Fig. 18 at -0.5 cycles (1000 km)$^{-1}$ and the gray lines are from the $n = 1$, $m = 2$ Rossby wave single-mode projection model at -0.5 cycles (1000 km)$^{-1}$ in Fig. 18.

ber–frequency regime of observed TIWs. This is because the mean currents in the single-mode projection model fail to speed up the altered $n = 1$, $m = 2$ Rossby wave sufficiently.

When fully developed, TIWs are nonlinear (Kennan and Flament 2000). The linear model used here therefore cannot be expected to quantitatively describe the precise structure of the TIWs across the entire Pacific or throughout the 9-month TIW season. Another shared deficiency of linearized stability analyses is the need for a prescribed mean current profile. In practice, the mean current is not known or even well defined since the background currents evolve considerably over the course of a TIW season because of external forcing and energy transfer to TIWs. The sensitivity of TIWs to changes in the background currents is examined in detail by J. M. Lyman and D. B. Chelton (2004, unpublished manuscript).

The projection model was applied here to study TIWs in the Pacific from POCM. Other regions, such as the equatorial Atlantic, have yet to be explored. Ultimately, the mean current profiles used in the projection model will be obtained from in situ data, rather than from POCM. The resulting eigenfunctions can then be compared with TOPEX/Poseidon observations of SSH. The projection model can also be applied to investigate the effects of mean currents on stable low-frequency Rossby waves. A longer-term goal is to understand the nonlinear dynamics of TIWs and the physical processes that control their equilibration and decay.

Acknowledgments. The research summarized in this manuscript was supported by the National Aeronautics and Space Administration under contracts 1206715 and 1217722 from the Jet Propulsion Laboratory. Roger M. Samelson was supported by NSF Grant oce-990784. John M. Lyman gratefully acknowledges support from National Research Council during this research; additional support was provided by the NOAA offices of Ocean and Atmospheric Research and the

NOAA Office of Global Programs during preparation of this manuscript. Helpful comments were provided by Jeffrey A. Proehl and Eric S. Johnson.

APPENDIX A

Vertical Structure

The baroclinic eigenfunctions $\psi_n(z)$ used in this paper are derived from the usual equation

$$\frac{\partial}{\partial_z}\left(\frac{1}{N^2}\frac{\partial\psi_n}{\partial_z}\right) = \frac{-1}{c_n^2}\psi_n, \tag{A1}$$

where

$$-\frac{1}{c_n^2} = \text{the eigenvalue for mode } n,$$

$$\psi_n = \text{the eigenfunction for mode } n,$$

c_n is the baroclinic phase speed, and $N^2(z)$ is the square of buoyancy frequency (Gill 1982), subject to the boundary conditions

$$\frac{\partial\psi_n}{\partial_z} = 0 \text{ at } z = 0 \text{ and } z = -H, \tag{A2}$$

where H is the depth of the water column.

The buoyancy frequency $N(z)$ in (A1) is obtained from the average geostrophically balanced buoyancy frequency N_G, which is computed by meridional integration of the thermal wind equation:

$$N_G^2(y, z) = N_o^2(z) - \int_{Y_S}^{Y_N} U_{zz}(y, z)\, dy, \tag{A3}$$

where Y_S is the southern boundary, Y_N is the northern boundary, $U(y, z)$ is the mean background zonal velocity, and N_o is some initial buoyancy frequency; N_o^2 is determined such that the square of the differences between N_G^2 and the squared buoyancy frequency determined from the model salinity and temperature, $N_{\text{pocm}}^2(y,z)$, are minimized. The integral

$$\int_{Y_S}^{Y_N} (N_G^2 - N_{\text{pocm}}^2)^2\, dy \tag{A4}$$

is thus minimized with respect to N_o^2 to obtain a least squares estimate of N_o^2. The resulting value of N_o^2 is then used to calculate N_G^2. Last, $N^2(z)$ is obtained from the meridional average of N_G^2 from 5°S to 5°N. Examples of the corresponding first two baroclinic modes are shown in Fig. A1.

APPENDIX B

The Two-Layer Reduced-Gravity Model

A two-layer, reduced-gravity model is the simplest representation of baroclinic equatorial dynamics (Gill 1982). In the case in which the equations of motion have been linearized about a mean upper-layer zonal velocity $U_o(y)$, which is in geostrophic equilibrium with mean layer thickness $H(y)$, and are subject to a rigid-lid approximation and the Boussinesq approximation, the two-layer reduced-gravity model takes the matrix form

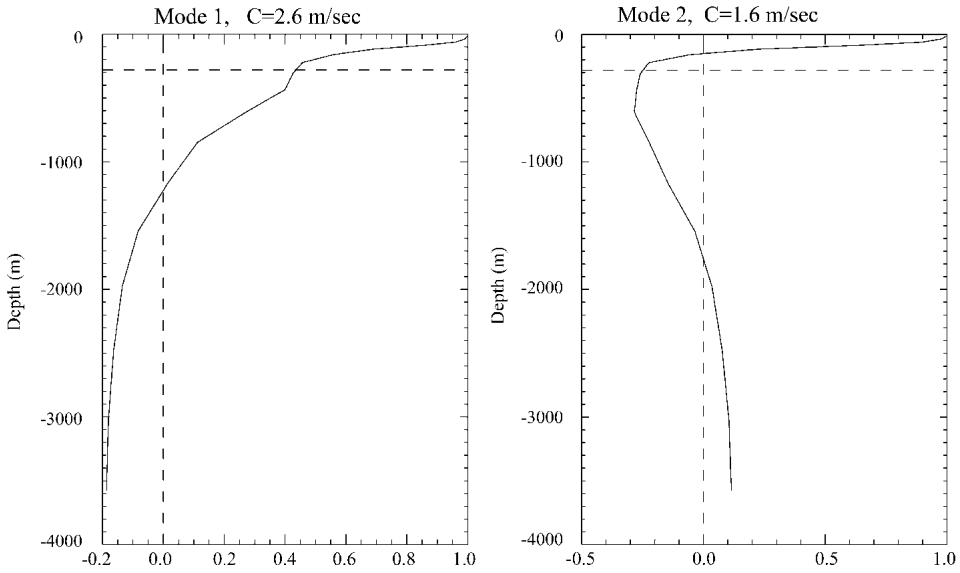

FIG. A1. The (left) first and (right) second baroclinic vertical eigenfunctions used in the projection model. The phase speeds of these two modes are 2.6 and 1.6 m s^{-1}, respectively.

$$\begin{bmatrix} U_o(y)k & i\left(\beta y - \dfrac{\partial U_o}{\partial y}\right) & \dfrac{1}{\rho_*}k \\ -i\beta y & U_o(y)k & -\dfrac{i}{\rho_*}\dfrac{\partial}{\partial y} \\ g'\rho_* H(y)k & -ig'\rho_*\left\{\dfrac{\partial H}{\partial y} + H(y)\dfrac{\partial}{\partial y}\right\} & U(y)_o k \end{bmatrix} \begin{bmatrix} u \\ v \\ p \end{bmatrix} = \omega \begin{bmatrix} u \\ v \\ p \end{bmatrix}, \tag{B1}$$

where

η = the perturbation sea surface height,

g' = the reduced gravity,

$U_o(y)$ = the mean flow in the upper layer,

$H(y)$ = the upper-layer thickness,

and the state variables u, v, and η are assumed to be a traveling wave of the form $e^{i(kx-\omega t)}$.

REFERENCES

Baturin, N. G., and P. P. Niiler, 1997: Effects of instability waves in the mixed layer of the equatorial Pacific. *J. Geophys. Res.,* **102,** 21 771–21 793.

Chelton, D. B., F. J. Wentz, C. L. Gentemann, R. A. deSzoeke, and M. G. Schlax, 2000: Satellite microwave SST observation of transequatorial tropical instability waves. *Geophys. Res. Lett.,* **27,** 1239–1242.

——, M. G. Schlax, S. K. Esbensen, N. Thum, M. H. Freilich, F. J. Wents, C. L. Gentemann, and M. J. McPhaden, 2001: Observations of coupling between surface wind stress and sea surface temperature in the eastern tropical Pacific. *J. Climate,* **14,** 1479–1498.

Contreras, R. F., 2002: Long-term observations of tropical instability waves. *J. Phys. Oceanogr.,* **32,** 2715–2723.

Cox, M. D., 1980: Generation and propagation of 30-day waves in a numerical model of the Pacific. *J. Phys. Oceanogr.,* **10,** 1168–1186.

Donohue, K. A., and M. Wimbush, 1998: Model results of flow instabilities in the tropical Pacific Ocean. *J. Geophys. Res.,* **103,** 21 401–21 412.

Flament, P. J., S. C. Kennan, R. A. Knox, P. P. Niiler, and R. L. Bernstein, 1996: The three-dimensional structure of an upper ocean vortex in the tropical Pacific Ocean. *Nature,* **383,** 610–613.

Flierl, G. R., 1978: Models of vertical structure and the calibration of two-layer models. *Dyn. Atmos. Oceans,* **2,** 341–381.

Gill, A. E., 1982: *Atmosphere–Ocean Dynamics.* Academic Press, 662 pp.

Guenther, R. B., and J. W. Lee, 1988: *Partial Differential Equations of Mathematical Physics and Integral Equations.* Prentice Hall, 544 pp.

Halpern, D., R. A. Knox, and D. S. Luther, 1988: Observations of 20-day meridional current oscillations in the upper ocean along the Pacific equator. *J. Phys. Oceanogr.,* **18,** 1514–1534.

Hansen, D. V., and C. A. Paul, 1984: Genesis and effects of long waves in the equatorial Pacific. *J. Geophys. Res.,* **89,** 10 431–10 440.

Harvey, R. R., and W. C. Patzert, 1976: Deep current measurements suggest long waves in the eastern equatorial Pacific. *Science,* **193,** 883–885.

Hashizume, H., S.-P. Xie, W. T. Liu, and K. Takeuchi, 2001: Local and remote atmospheric response to tropical instability waves: A global view from space. *J. Geophys. Res.,* **106,** 10 173–10 185.

Kennan, S. C., 1997: Observations of a tropical instability vortex. Ph.D. thesis, University of Hawaii at Manoa, 190 pp.

——, and P. J. Flament, 2000: Observations of a tropical instability vortex. *J. Phys. Oceanogr.,* **30,** 2277–2301.

Legeckis, R., 1977: Long waves in the eastern equatorial Pacific Ocean: A view from a geostationary satellite. *Science,* **197,** 1179–1181.

——, 1986: Long waves in the equatorial Pacific and Atlantic Oceans during 1983. *Ocean–Air Interactions,* **1,** 1–10.

——, E. Pichel, and G. Nesterczuk, 1983: Equatorial long waves in geostationary satellite observation and in a multichannel sea surface temperature analysis. *Bull. Amer. Meteor. Soc.,* **64,** 133–139.

Luther, D. S., and E. S. Johnson, 1990: Eddy energetics in the upper equatorial Pacific during Hawaii-to-Tahiti Shuttle Experiment. *J. Phys. Oceanogr.,* **20,** 913–944.

Lyman, J. M., 2002: The cross-equatorial structure of tropical instability waves in sea surface height. Ph.D. thesis, Oregon State University, 134 pp.

Malardé, J. P., P. D. Mey, C. Périgaud, and J. F. Minster, 1987: Observations of long equatorial waves in the Pacific Ocean by *Seasat* altimetry. *J. Phys. Oceanogr.,* **17,** 2273–2279.

Mallat, S., 1999: *A Wavelet Tour of Signal Processing.* 2d ed. Academic Press, 620 pp.

Masina, S., G. Philander, and A. Bush, 1999a: An analysis of tropical instability waves in a numerical model of the Pacific Ocean. Part II: Generation and energetics. *J. Geophys. Res.,* **104,** 29 637–29 662.

——, ——, and ——, 1999b: An analysis of tropical instability waves in a numerical model of the Pacific Ocean. Part I: Spatial variability. *J. Geophys. Res.,* **104,** 29 613–29 636.

McClean, J. L., A. J. Semtner, and V. Zlotnicki, 1997: Comparisons of mesoscale variability in the Semtner-Chervin 1/4° model, the Los Alamos Parallel Ocean Program 1/6° model, and TOPEX/Poseidon data. *J. Geophys. Res.,* **102,** 25 203–25 226.

McCreary, J. P., and Z. Yu, 1992: Equatorial dynamics in a 2.5-layer model. *Progress in Oceanography,* Vol. 29, Pergamon, 61–132.

McPhaden, M. J., 1996: Monthly period oscillations in the Pacific North Equatorial Countercurrent. *J. Geophys. Res.,* **101,** 6337–6359.

Menkes, C., J.-P. Boulanger, and A. J. Busalacchi, 1996: Evaluation of TOPEX and basin-wide Tropical Ocean and Global Atmosphere-Tropical Atmosphere Ocean sea surface topographies and derived geostrophic currents. *J. Geophys. Res.,* **101,** 25 087–25 099.

Musman, S., 1989: Sea height wave form in equatorial waves and its interpretation. *J. Geophys. Res.,* **94,** 3303–3309.

Périgaud, C., 1990: Sea level oscillations observed with *Geosat* along the two shear fronts of the Pacific North Equatorial Countercurrent. *J. Geophys. Res.,* **95,** 7239–7248.

Philander, S. G. H., 1976: Instabilities of zonal equatorial currents. *J. Geophys. Res.,* **81,** 3725–3735.

——, 1978: Instabilities of zonal equatorial currents, 2. *J. Geophys. Res.,* **83,** 3679–3682.

——, W. J. Hurlin, and R. C. Pacanowski, 1986: Properties of long equatorial waves in models of the seasonal cycle in the tropical Atlantic and Pacific Oceans. *J. Geophys. Res.,* **91,** 14 207–14 211.

Proehl, J. A., 1991: On the numerical dispersion relation of equatorial waves. *J. Geophys. Res.,* **96,** 16 929–16 934.

——, 1998: The role of meridional flow asymmetry in the dynamics of tropical instability. *J. Geophys. Res.,* **103,** 24 597–24 618.

Pullen, P. E., R. L. Bernstein, and D. Halpern, 1987: Equatorial long-wave characteristics determined from satellite sea surface temperature and in situ data. *J. Geophys. Res.,* **92,** 742–748.

Qiao, L., and R. H. Weisberg, 1995: Tropical instability wave kinematics: Observations from the Tropical Instability Wave Experiment. *J. Geophys. Res.,* **100,** 8677–8693.

——, and ——, 1998: Tropical instability wave energetics: Observations from the Tropical Instability Wave Experiment. *J. Phys. Oceanogr.,* **28,** 345–360.

Semtner, A. J. J., and R. M. Chervin, 1992: Ocean general circulation from a global eddy-resolving model. *J. Geophys. Res.,* **97,** 5493–5550.

Stammer, D., 1997: Steric and wind-induced changes in TOPEX/Poseidon large-scale sea surface topography observations. *J. Geophys. Res.,* **102,** 20 987–21 009.

Strutton, P. G., J. P. Ryan, and F. P. Chavez, 2001: Enhanced chlorophyll associated with tropical instability waves in the equatorial Pacific. *Geophys. Res. Lett.,* **28,** 2005–2008.

Weidman, P. D., D. L. Mickler, B. Dayyani, and G. H. Born, 1999: Analysis of Legeckis eddies in the near-equatorial Pacific. *J. Geophys. Res.,* **104,** 7865–7887.

Wyrtki, K., and Coauthors, 1981: The Hawaii to Tahiti shuttle experiment. *Science,* **211,** 22–28.

Xie, S.-P., M. Ishiwatari, H. Hashizume, and K. Takeuchi, 1998: Coupled ocean-atmospheric waves on the equatorial front. *Geophys. Res. Lett.,* **25,** 3863–3866.

Yu, Z., J. P. McCreary, and J. A. Proehl, 1995: On the meridional asymmetry and energetics of tropical instability waves. *J. Phys. Oceanogr.,* **25,** 1680–1686.